CrossMark

JFM PAPERS

The late start of the mean velocity overlap log law at $y^+ = O(10^3)$ – a generic feature of turbulent wall layers in ducts

Peter A. Monkewitz†

Faculty of Engineering Science, École Polytechnique Fédérale de Lausanne (EPFL), CH-1015, Lausanne, Switzerland

One of the key observations in the Princeton Superpipe was the late start of the logarithmic mean velocity overlap layer at a wall distance of the order of 10^3 inner units. Between $y^+ \approx 150$, the start of the overlap layer in zero pressure gradient turbulent boundary layers, and $y^+ \approx 500$, the Superpipe profile is modelled equally well by a power law or a log law with a larger slope than in the overlap layer. This paper demonstrates, that the asymptotic mean velocity profile in turbulent plane channel flow exhibits analogous characteristics, namely a rather sudden decrease of logarithmic slope (increase of κ) at a y^+ of approximately 600, which marks the start of the actual overlap layer. The demonstration results from the first construction of the complete mean velocity inner and outer asymptotic expansions up to order $O(Re_\tau^{-1})$ from direct numerical simulations (DNS) at moderate Reynolds numbers. The $O(Re_\tau^{-1})$ contribution to the indicator function $\Xi^+ = y^+ (\mathrm{d}U^+/\mathrm{d}y^+)$ is found to be important and to prevent the direct determination of κ from currently available channel DNS. A preliminary, leading-order analysis of a Couette flow DNS, on the other hand, yields an increase of logarithmic slope (decrease of κ) at a $y^+_{break} \approx 400$. The correlation between the sign of the slope change and the flow symmetry motivates the hypothesis that the breakpoint between the possibly universal short inner logarithmic region and the actual overlap log-law corresponds to the penetration depth of large-scale turbulent structures originating from the opposite wall.

Key words: boundary layer structure

1. Aim of the study and some comments on the asymptotic analysis of mean velocity profiles

For over 100 years, enormous efforts have been made to better understand the physics of turbulent wall-bounded flows and numerous approaches have been pursued. One of

† Email address for correspondence: peter.monkewitz@epfl.ch

them consists of subdividing the turbulent boundary layer according to the dominant balance in the governing equations and to consider reduced models in the different layers. The papers of Wei *et al.* (2005) and Klewicki (2013) are examples for this approach. Another angle on the problem has been provided by symmetry-based turbulence theory, presented for instance in Oberlack (2001). Still another approach is what may be called the 'building block approach', where ensembles of relatively simple basic flow structures are arranged in the wall layer such as to reproduce specific measured or computed flow statistics. A prominent example of this approach is the so-called 'attached eddy model' recently reviewed by Marusic & Monty (2019). While these approaches are all different, they generally have the common aim of modelling and/or explaining the asymptotic, high Reynolds number structure of turbulence statistics, in particular of the mean velocity profile, in the following abbreviated MVP, but are developed, calibrated and tested on finite Reynolds number data. Hence, the question of whether a model correctly reproduces the infinite Reynolds number limit is a difficult one, which has fuelled numerous controversies.

The present study aims to provide some answers to the above question by unifying the modelling of high Reynolds number MVPs in terms of asymptotic expansions for the three 'canonical' turbulent parallel flows: pipe, plane channel and plane Couette flows, i.e. flows which are in the mean homogeneous in both the streamwise and azimuthal/spanwise directions. All three flows are characterized by a single 'outer' or global length scale $\check{L}$, the pipe radius or channel half-width and a constant wall shear stress $\check{\tau}_w$, where $\breve{}$ identifies dimensional quantities throughout the paper. In the following, the classical two-layer description is adopted with the standard 'inner' or viscous length scale $\check{\ell} \equiv (\check{\nu}/\check{u}_\tau)$, where $\check{u}_\tau \equiv (\check{\tau}_w/\check{\rho})^{1/2}$, $\check{\rho}$ and $\check{\nu}$ are the friction velocity, density and dynamic viscosity, respectively. The relevant Reynolds number is the 'friction Reynolds number' $Re_\tau \equiv \check{L}/\check{\ell}$.

To date, only the Princeton Superpipe MVPs (Zagarola & Smits 1997, 1998; McKeon 2003; McKeon *et al.* 2004), reviewed in § 2.1, were acquired at high enough Reynolds numbers to reveal the detailed structure of the region, which links the wall layer to the core. The characteristic feature of this region for friction Reynolds numbers Re_τ beyond approximately 30 000 – a distinct reduction of (logarithmic) slope at a wall distance well beyond the start of the log law in zero pressure gradient turbulent boundary layers (abbreviated ZPG TBLs) – is reviewed in § 2.1. In § 2.2, the hypothesis is advanced that this feature is related to turbulent structures, which originate from the opposite wall. The outline of the more technical continuation of the paper is postponed to § 2.3.

Since the interpretation of channel and Couette flow experiments is complicated by the finite spanwise extent of facilities (see e.g. Vinuesa, Schlatter & Nagib 2018), attention is turned to direct numerical simulations (DNS). However, the Reynolds numbers for the available DNS are relatively low, such that the contamination of the overlap MVP by both its inner and outer parts remains a problem. The 'Reynolds number handicap' of DNS is overcome by a methodology to formally extrapolate finite Reynolds number profiles of the MVP or any other turbulence statistics to infinite Reynolds number. This is achieved by constructing at least two terms of the large Reynolds number composite asymptotic expansion from high quality profiles at different Reynolds numbers. Identifying the multi-term composite expansion with the DNS profile, one arrives at a good representation of the infinite Reynolds limit by subtracting all the higher-order terms of the composite expansion from the DNS.

However, before getting into the technical details of constructing such expansions from DNS, it is useful to review some basic principles of matched asymptotic expansions (MAE, see for instance the excellent monograph by Kevorkian & Cole 1981) and their application to wall turbulence, reviewed, for instance, by Panton (2005).

Within the framework of MAE, the non-dimensional mean velocity $U^+ \equiv \breve{U}/\breve{u}_\tau$ at large Re_τ is modelled by inner and outer asymptotic expansions $U_{in}^+(y^+) = \sum \phi_n(Re_\tau)f_n(y^+)$ and $U_{out}^+(Y) = \sum \Phi_n(Re_\tau)F_n(Y)$, where $y^+ \equiv \breve{y}/\breve{\ell}$ and $Y \equiv \breve{y}/\breve{L} = y^+/Re_\tau$ are the inner-scaled and outer-scaled non-dimensional wall-normal coordinates, while $\phi_n(Re_\tau)$ and $\Phi_n(Re_\tau)$ are suitable gauge functions. These inner and outer expansions for U^+ have to be matched in an 'overlap' layer, where $(y^+ Y)$ is of order unity.

This overlap layer is, however, not a third layer on the same footing as inner and outer layers, but the 'intersection' or the common part of the inner and outer expansions. As its name suggests, it only contains terms that are common to both inner and outer expansions and their number depends therefore on how many terms are retained in the two expansions to be matched. This precise definition allows to construct the additive composite profile, which is the sum of inner and outer expansions minus the common part, as the latter is counted twice in the sum.

An important corollary to this statement is that the common part contains no new physics, unless it is introduced by an additional reasoning. The classical example in the present context is the postulate of asymptotic independence of inner and outer scales by Millikan (1938) (see also the early formulation by von Kármán 1930), from which it follows that, in the overlap layer, $y^+(\mathrm{d}U^+/\mathrm{d}y^+) = Y(\mathrm{d}U^+/\mathrm{d}Y)$ can only be a constant κ^{-1}. This physical argument yields directly the functional form of the leading-order common part, the log law

$$U_{cp,0}^+ = \kappa^{-1}\ln(y^+) + B = \kappa^{-1}\ln(Re_\tau) + \kappa^{-1}\ln(Y) + B. \tag{1.1}$$

A first remark concerns the log law in outer variables, which contains both order $O(1)$ terms and a $\ln(Re_\tau)$. Therefore, it must be regarded as of 'block order' unity, where the block order, introduced by Crighton & Leppington (1973), regroups all the terms of order $Re_\tau^n \ln^m(Re_\tau)$ with different m values into a single block order Re_τ^n. This is also seen in the 'law of the wake' of Coles (1956), $U_{out,0}^+ = \kappa^{-1}\ln(Re_\tau) + \kappa^{-1}\ln(Y) + B + 2\pi\kappa^{-1}f(Y)$, which is one way of writing the leading term of the outer expansion.

The reported value of κ in (1.1) has varied considerably between different flows and over time, from the 0.38 originally estimated by von Kármán (1930) to the 'popular' value of 0.41 (see for instance (Pope 2000), § 7.3.3) to 0.436 in the Superpipe (Zagarola & Smits 1998) and the CICLoPE pipe (Fiorini 2017; Nagib *et al.* 2017, 2019) (see also the extensive discussion in Marusic *et al.* 2010).

The diversity of κ values should, however, not come as a surprise, since the Millikan argument does in no way preclude the dependence of κ and B in (1.1) on control parameters, such as for instance the pressure gradient parameter $\beta \equiv -\breve{L}(\partial\breve{p}/\partial\breve{x})(\breve{\tau}_w)^{-1}$ ($\beta = 0$, 1 and 2 for Couette, channel and pipe flow, respectively) and geometry (see e.g. Nagib & Chauhan 2008). Furthermore, its value in different flows is still difficult to pin down because the κ values extracted from high Reynolds number experiments come with a significant uncertainty (see e.g. Bailey *et al.* 2014), while the Re_τ of high quality DNS are still too low to produce clean log laws.

Possibly because of this uncertainty, κ has retained an aura of fundamental constant, the Kármán 'constant', and prompted considerable attention to higher-order terms in the overlap region by, among others, Yajnik (1970), Afzal & Yajnik (1973), Jiménez & Moser (2007) and most recently by Luchini (2017, see appendix B for a critical appraisal).

The main points on asymptotic matching and common parts may be summarized as follows:

(i) The logarithm in the leading-order overlap profile for U^+ ((1.1)) is a consequence of the postulated asymptotic independence of inner and outer scales and hence of physical origin.

(ii) It follows directly from Coles' law of the wake (1956), that the κ values determined from the leading-order overlap profile and the leading-order centreline velocity $U_{cl,0}^+(Re_\tau) = \kappa^{-1}\ln(Re_\tau) + C$ must be identical!

(iii) Higher-order terms in the common part depend entirely on which terms are included in the inner and outer expansions, as they must be contained in both the limits $y^+ \gg 1$ of the inner and $Y \ll 1$ of the outer expansion.

(iv) While composite asymptotic expansions with a given finite number of terms are constructed to approach the exact solution in the limit of infinitely large Re_τ, they often 'work' surprisingly well at lower Re_τ. However, as the inner–outer scale separation diminishes, the underlying overlap profile (equation (1.1) in the present context) becomes progressively 'buried' by the superposed inner and outer profiles. In other words, it can no longer be readily identified in the composite profile and needs to be educed by a proper asymptotic analysis.

2. Reconciling the MVP characteristics in the Princeton Superpipe with plane channel and Couette profiles

2.1. *The principal characteristics of the mean velocity overlap profile in the Superpipe*

Until the Princeton Superpipe experiment of Zagarola & Smits (1997, 1998), the 'standard model' of the MVP in wall-bounded turbulent flows consisted of inner and outer profiles, monotonically connected by the logarithmic overlap profile extending from $y^+ \approx 150$ to $Y \approx 0.2$, except for a small overshoot centred around $y^+ \approx 30$ (see Nagib & Chauhan (2008) and appendix A). It goes without saying that the extent of the overlap region depends on how much deviation from the pure log law is tolerated.

The challenge to this 'standard model' by the Princeton Superpipe experiment has been twofold:

(i) The originally reported κ of 0.436, as well as the revised value of 0.421, obtained by McKeon *et al.* (2004) with smaller Pitot probes and a different correction scheme have attracted a great deal of scepticism. Based on the extensive collection of centreline velocities U_{cl}^+ minus the fit $\kappa^{-1}\ln(Re_\tau) + C$ in figure 1 for the two different κ values and corresponding C values, the pipe overlap κ can be placed in the bracket [0.42, 0.44]. With the present data, it is not possible to pinpoint it more precisely (see e.g. Bailey *et al.* 2014). It is, however, clear that the Superpipe κ and the preliminary values from the CICLoPE facility (Fiorini 2017; Nagib *et al.* 2017, 2019) are different from the κ in ZPG TBLs, which has converged to approximately 0.384 (see for instance Monkewitz, Chauhan & Nagib 2007; Marusic *et al.* 2010). However, in light of the comments on the Millikan matching argument in § 1, these differences should not come as a surprise as they do not violate any basic principles.

(ii) More importantly, the overlap log law was found to start only beyond $y^+ \gtrsim 500$, much further from the wall than in the ZPG TBL, where a clean log law is observed for $y^+ \gtrsim 150$ (see for instance Monkewitz *et al.* 2007; Marusic *et al.* 2010). Surprisingly, this feature of the Superpipe profiles has gone largely uncommented and certainly unexplained. Originally, both Zagarola & Smits (1998) and McKeon *et al.* (2004) have fitted U^+ in the interval $150 \lesssim y^+ \lesssim 500$ with power laws, but
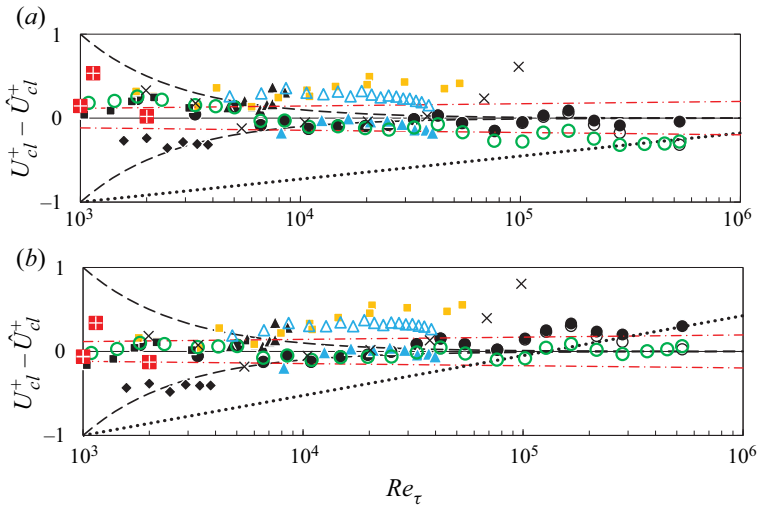
Figure 1. Pipe centreline velocities minus $\kappa^{-1}\ln(Re_\tau) + C$ versus Re_τ for (*a*) $\kappa = 0.42$, $C = 6.84$ and (*b*) $\kappa = 0.436$, $C = 7.65$. ●, Superpipe data corrected according to McKeon; ○, same data without roughness correction; ○ (green), Superpipe data of Zagarola & Smits (1997) with same roughness correction; ×, Superpipe NSTAP data of Hultmark *et al.* (2012); ◆, Perry & Abell (1977); ▲, Zanoun *et al.* (2007); ■, Monty (2005); △△△ (blue), CICLoPE data of Fiorini (2017); ▲▲▲ (blue), new CICLoPE data of Nagib *et al.* (2019); ■■■ (yellow), figure 6 of Furuichi *et al.* (2018); ■ (red), the three DNS of El Khoury *et al.* (2013) ($Re_\tau = 999$), Wu & Moin (2008) ($Re_\tau = 1142$) and Chin, Monty & Ooi (2014) ($Re_\tau = 2003$). $\cdot - \cdot$ (red), $\pm 0.5\,\%$ of reference $\hat{U}_{cl}^+$; - - -, $\pm 10^3/Re_\tau$; $\cdots$, slope corresponding to $\kappa = 0.40$.

McKeon (2003) noted that a logarithm with slope $1/0.385$ also 'fits quite well'. Consistent with this observation, the hypothesis (2.1) and the analysis of § 3.3, both the near-wall and the overlap region will be modelled by logarithmic laws with log slopes of $(1/\kappa_M)$ and $(1/\kappa)$, respectively, and a rather sharp transition between the two at a y_{break}^+ of approximately 500 (note that the 'M' in κ_M indicates that it is the κ used to generate the inner Musker profile of appendix A).

(iii) Based on velocity measurements with the miniature 'NSTAP' hot-wires in the Princeton Superpipe, Marusic *et al.* (2013) have put the breakpoint y_{break}^+, i.e. the start of the logarithmic overlap region, at $y_{break}^+ \approx 3Re_\tau^{1/2}$. On the other hand, Monkewitz (2017) found that, based on the original Pitot measurements, the slope change correlated better with a fixed $y_{break}^+ \approx 500$. At the Re_τ considered, these two scalings for the start of the overlap log law are numerically similar and within the uncertainty of the breakpoint location. However, the scaling on the intermediate variable $y^+ Re_\tau^{-1/2}$ poses a problem: if the inner profile for $y^+ < y_{break}^+$ is a function of y^+ alone, as observed, the additive log-law constant B can no longer be constant, but increases with $\ln(Re_\tau)$. Furthermore, the comparison of the two scalings over the full Superpipe Reynolds number range by Monkewitz (2019) clearly favours a constant y_{break}^+, which is therefore adopted in the following.

The main Superpipe findings, detailed above, are illustrated in figure 2 by model profile adapted from Monkewitz (2017) to fit the partial velocity profiles obtained by Fiorini (2017) in the CICLoPE pipe with traditional 1 and 1.1 mm hot-wires and his centreline Pitot data. Note that, in this figure, and in the rest of the paper, profile fits are identified by hats ˆ, while experimental or DNS profiles have no hat.

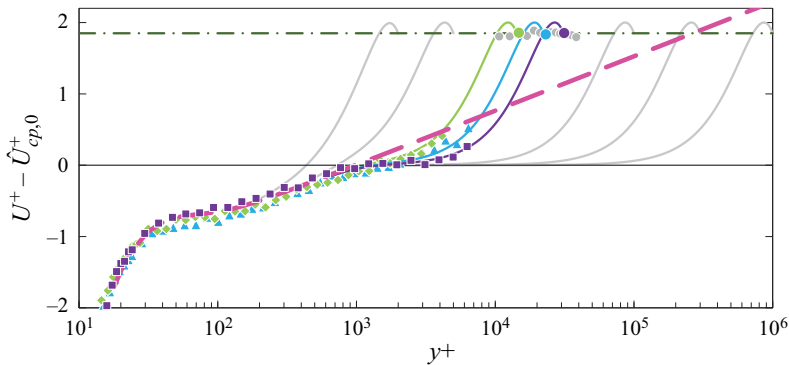Figure 2. Pipe mean velocity profiles minus leading-order overlap or common part $\hat{U}_{cp,0}^{+} = (1/0.44)\ln(y^{+}) + 6.34$. ♦♦ (lime green), ▲▲ (sky blue), ■■ (violet), hot-wire data of Fiorini (2017) for $Re_{\tau} = 14.3, 22.2, 31.0 \times 10^{3}$. — (lime green), — (sky blue), — (violet), corresponding model profiles, composed of the inner Musker profile $\hat{U}_{M}^{+}(y^{+}; 0.384, 4.05)$ ((A1)), the original 'hump' $\hat{H}_{NC}(y^{+}; 0.351, 1, 30)$ ((A7)), a change of log slope at $y_{break}^{+} = 10^{3}$ to the common part $\hat{U}_{cp,0}^{+}$, and an outer part adapted from Monkewitz (2017). - - - (magenta), Musker profile with hump minus $\hat{U}_{cp,0}^{+}$. — (grey), additional model profiles for $Re_{\tau} = 2, 5, 100, 300, 1000 \times 10^{3}$. ● (grey), centreline Pitot data of Fiorini (2017), with ● (lime green), ● (sky blue), ● (violet), data for $Re_{\tau} = 14.8, 23.2, 31.4 \times 10^{3}$, close to the Re_{τ} of the hot-wire profiles. — · —, centreline velocity fit $\hat{U}_{cl,0}^{+} - \hat{U}_{cp,0}^{+} = 1.85$.

These hot-wire data are consistent with an increase of κ by $\cong 0.05$ around a breakpoint $y_{break}^{+} \cong 10^{3}$, which becomes apparent in the MVP beyond a Re_{τ} of approximately 30 000. The main profile parameters fitting the data of Fiorini (2017) are seen to be close to the ones of Zagarola & Smits (1997, 1998), but one will have to wait for an upgraded CICLoPE instrumentation to narrow down the uncertainty of κ_{M}, y_{break}^{+} and κ (see Nagib *et al.* 2017, 2019). For the prospect of using DNS, see § 4.2.

The Superpipe results described above were met with scepticism, to say the least, and the interrogations were numerous: the question of corrections for wall roughness was brought up by Perry, Hafez & Chong (2001) and finally resolved by Allen, Shockling & Smits (2005). The diverse Pitot probe corrections were questioned and prompted a vast investigation by an international collaboration (Bailey *et al.* 2013). Finally, the effect of Pitot tube positioning errors was considered by Vinuesa, Duncan & Nagib (2016). In the end, the Superpipe results have withstood all these additional investigations, and so one has to ask whether the MVP in other ducted parallel flows, in particular plane channel and Couette flow, will also exhibit the Superpipe features of figure 2 if pushed to higher Reynolds numbers. This author cannot conceive of any reason for this not to be the case, and so the Superpipe mean velocity structure is expected to also emerge at higher Re_{τ} in plane channel and Couette flows. Before demonstrating that this is the case, it is helpful to think of a coherent explanation for the difference between the logarithmic regions in ZPG TBLs and ducted parallel flows. Such a possible explanation is proposed in § 2.2.

2.2. *Hypothesis on the effect of the opposite wall*

The following explanation is proposed for both the late start of the overlap log law and the flow dependence of the overlap κ in simple ducted parallel flows, illustrated in figure 2 for pipe flow:
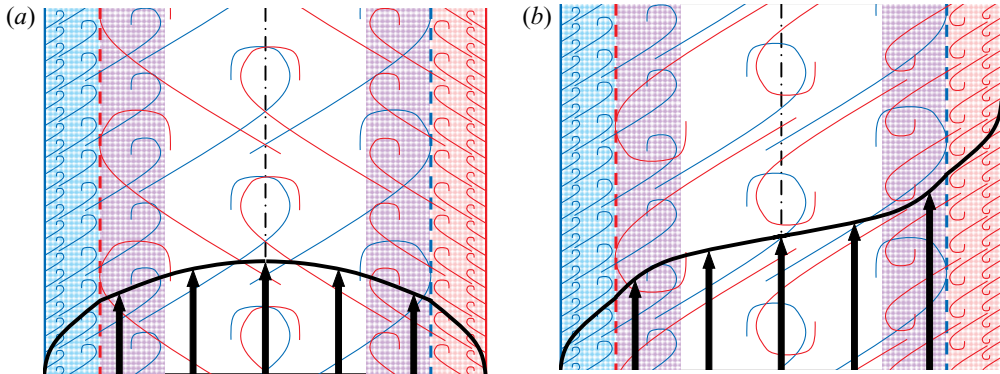
Figure 3. Cartoons illustrating the hypothesis 2.1. Red and blue shaded areas: wall layers not affected by the opposite wall; violet shade: overlap layers affected by 'eddies' originating from the opposite wall. (*a*) Overlap logarithmic slope reduced relative to the wall layers for pipe and channel flows; (*b*) overlap logarithmic slope increased relative to the wall layer for Couette flow.

HYPOTHESIS 2.1. *The breakpoint* y^+_{break}*, separating the short logarithmic region with slope* $(1/\kappa_M)$ *between* $y^+ \approx 150$ *and* y^+_{break} *and the true overlap log-law with Kármán parameter* κ*, corresponds to the penetration depth of large-scale turbulent structures originating from the opposite wall.*

This hypothesis (2.1) is visualized by the cartoon of figure 3 and has two testable consequences:

  (i) In pipe and channel flows the disturbances of opposite vorticity emanating from the opposite wall reduce dU^+/dy^+ for $y^+ > y^+_{break}$ and hence $\kappa > \kappa_M$. Conversely, in Couette flow these vorticity disturbances must increase the mean shear outside of y^+_{break}, leading to $\kappa < \kappa_M$.
  (ii) At sufficiently high Re_τ, the short logarithmic layer with slope $(1/\kappa_M)$ is possibly not influenced by geometry and the inner layer $0 \le y^+ \le y^+_{break}$ may therefore be universal, at least for the truly parallel flows considered here.

Finding a theoretical underpinning for the above hypothesis or an alternative explanation is left for future research. For this, the variance of vorticity components in the simulations of Lee & Moser (2015) may provide a lead, as it changes from a $1/y^+$ power-law decay to an exponential decay right around a y^+ of 10^3, independently of Re_τ.

2.3. *Outline of §§ 3–5*

In § 3, a number of high quality profiles for plane channel flow, up to $Re_\tau = 5186$ (Lee & Moser 2015), are used to construct, for the first time, the complete inner and outer asymptotic expansions of U^+ up to terms of order $O(Re_\tau^{-1})$. This allows the extraction of the leading-order MVP from DNS at low to moderate Re_τ values. In particular the leading-order inner profile $U^+_{in,0}$, obtained in § 3.3, corroborates the hypothesis (2.1) by revealing a clean break point at $y^+_{break} \cong 600$, around which the logarithmic slope of U^+ decreases from $(1/0.398)$ to $(1/0.42)$ over a short y^+-distance.

An analogous reconstruction of 2-term asymptotic expansions from available Couette DNS, on the other hand, has not been feasible. Limited to the leading-order inner and outer asymptotic expansions, it is nevertheless possible to demonstrate in § 4.1, that the

Couette DNS of Kraheberger, Hoyas & Oberlack (2018) for $Re_\tau = 1026$ does show the steepening of U^+ at y^+_{break}, corresponding to $\kappa = 0.367 < \kappa_M = 0.40$, in conformity with the hypothesis (2.1).

A brief review of three pipe DNS profiles in § 4.2 finally reveals, that the differences between available profiles are too large to attempt an analysis analogous to the one for the channel.

The paper closes with a recap of selected findings and a selection of open questions in § 5.

3. Higher-order asymptotic expansions of U^+ for the plane channel

At this point, the paper switches from phenomenology to a purely formal singular perturbation approach. The only assumptions for the following analysis are the restriction to the two classical inner and outer layers, connected through an overlap layer, which is at leading order of the physically motivated logarithmic form (1.1). However, no assumptions are made on the value of the Kármán parameter κ, nor on the exact location of the overlap layer.

3.1. *Methodology for extracting asymptotic expansions from DNS*

The objective is to obtain, for the plane channel, the inner and outer asymptotic expansions of the mean velocity U^+ up to and including the block order $O(Re_\tau^{-1})$ (see Crighton & Leppington (1973), and § 1 for the concept of block order)

$$U^+_{in}(y^+) = U^+_{in,0}(y^+) + Re_\tau^{-1} U^+_{in,1}(y^+) + O(Re_\tau^{-2}), \tag{3.1}$$

and

$$U^+_{out}(Y) = U^+_{out,0}(Y) + Re_\tau^{-1} U^+_{out,1}(Y) + O(Re_\tau^{-2}), \tag{3.2}$$

together with the common part U^+_{cp}, which can be expressed in terms of y^+, Y, or the intermediate variable $\eta = y^+ Re_\tau^{-1/2} = Y Re_\tau^{1/2}$. Identifying the composite expansion $U^+_{comp} = U^+_{in} + U^+_{out} - U^+_{cp}$ with U^+_{DNS}, the first two orders in the expansions (3.1) and (3.2) are successively determined for the first time and fitted by suitable functions.

Rather counter-intuitively, the determination of the inner and outer expansions is best started with the order $O(Re_\tau^{-1})$ terms. Between the wall and the overlap region, the deviation of the inner velocity ((3.1)) from the total velocity, taken to be $U^+_{DNS}(y^+)$, is of the order of $| U^+_{out}(Y) - U^+_{cp} |$. Hence, assuming that the asymptotic expansion (3.1) converges rapidly (an assumption justified *a posteriori*), one obtains a good estimate of $U^+_{in,1}(y^+)$ between the wall and the overlap layer by taking differences of two total velocity profiles at equal y^+ values (obtained by 3-point quadratic interpolation of the original DNS data) and different Re_τ values

$$[U^+_{DNS}(y^+; Re_{\tau,1}) - U^+_{DNS}(y^+; Re_{\tau,2})][Re_{\tau,1}^{-1} - Re_{\tau,2}^{-1}]^{-1}$$
$$= U^+_{in,1}(y^+) + O(Re_\tau^{-1}; | U^+_{out}(Y) - U^+_{cp} |). \tag{3.3}$$

Similarly, between the overlap region and the centreline, the outer velocity ((3.2)) is equal to the total velocity $U^+_{DNS}(Y)$, with an error of order $| U^+_{in}(y^+) - U^+_{cp} |$.

Profile	Re_τ	Colour in figures	Reference
#1	5186	■ (purple)	Lee & Moser (2015)
#2	2004	■ (sky blue)	Hoyas & Jiménez (2006)
#3	1000	■ (green)	Lee & Moser (2015)
#4	934	■ (spring green)	Del Álamo *et al.* (2004)

Table 1. Channel DNS profiles used to determine contributions of $O(Re_\tau^{-1})$.

However, obtaining the first-order term $U_{out,1}^+(Y)$ is a bit trickier, because the leading block order of the outer expansion (3.2) is of the well-known form

$$U_{out,0}^+(Y) = (1/\kappa)\ln(Re_\tau) + F(Y). \tag{3.4}$$

Two strategies to determine $U_{out,1}^+(Y)$ are pursued in § 3.2:

(i) The first is to assume κ in (3.4) and to use the analogue of (3.3) to determine $U_{out,1}^+(Y;\kappa)$. The 'true' $U_{out,1}^+(Y)$ is then obtained by iterating on κ until the best collapse of $U_{out,1}^+(Y)$ is obtained from different profile pairs.

(ii) The second, assumption-free strategy is to use a third DNS profile at a different Reynolds number to eliminate the $(1/\kappa)\ln(Re_\tau)$ term from the two DNS profiles at $Re_{\tau,1}$ and $Re_{\tau,2}$, before proceeding analogous to (3.3).

The strategies outlined above to educe higher-order terms from DNS, are fundamentally different from the attempts to determine higher-order terms in the overlap region, discussed in § 1. Here, $U_{in,1}^+(y^+)$ and $U_{out,1}^+(Y)$ are determined from the profiles in the inner wall region and the outer region near the centreline, respectively. Their proper matching in the overlap region only serves as an *a posteriori* verification.

The primary difficulty in implementing the above program is the required extraordinary fidelity of the DNS. Deviations from the Navier–Stokes solution must be sufficiently smaller than U^+/Re_τ in order to extract the $O(Re_\tau^{-1})$ terms with any kind of confidence, since profile uncertainties are amplified by a factor of the order of the smaller Re_τ used in (3.3). At first thought, one might wish for higher DNS Reynolds numbers in order to obtain a better separation of inner and outer scales and hence a clean(er) overlap log law. However, if the uncertainty of the DNS does not diminish at least as $1/Re_\tau$, nothing is gained for the determination of higher-order terms in the asymptotic expansion. In other words, it appears more important to improve the fidelity of DNS than to keep increasing the Reynolds number. Finally, it has to be kept in mind that the dependence of the U^+ profiles on additional parameters, such as the computational box size, has to be much weaker than its dependence on Re_τ.

The four DNS profiles listed in table 1 have been found to produce consistent results for both first-order terms $U_{in,1}^+$ and $U_{out,1}^+$ in the expansions (3.1) and (3.2), and will in the following be referred to by their profile number in the table. The principal computational characteristics of these DNS are summarized in table 1 of Lee & Moser (2015).

3.2. *The outer expansion $U_{out}^+(Y)$*

The first-order outer profile $U_{out,1}^+(Y)$ is determined with both methods discussed in § 3.1. Iterating on κ, until the best collapse of $U_{out,1}^+(Y;\kappa,i,j)$ determined from different profile
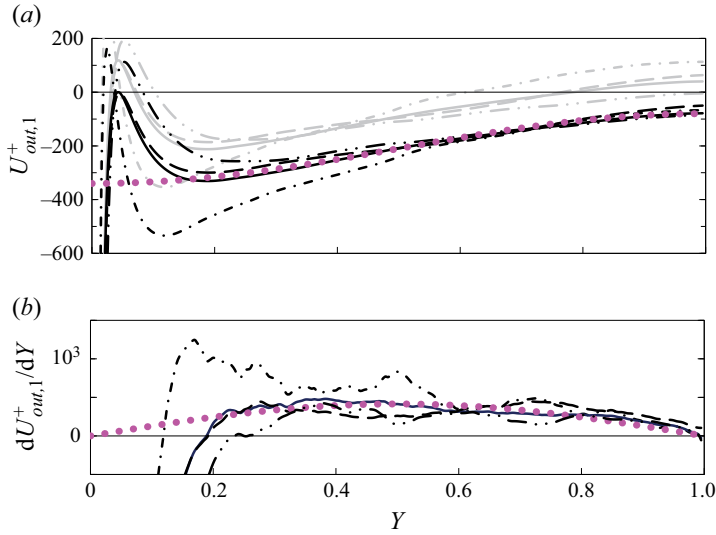
Figure 4. (*a*) Higher-order term $U_{out,1}^+(Y)$ of the outer expansion for the optimal $\kappa = 0.42$, obtained with pairs of DNS from table 1: —, (#1,#3); - - -, (#1,#4); — · —, (#1,#2); — · · —, (#2,#3); ● ● ● (magenta), fit by (3.5); grey: $U_{out,1}^+(Y)$ with same profile pairs, but $\kappa = 0.41$. (*b*) Derivative $\mathrm{d}U_{out,1}^+(Y)/\mathrm{d}Y$ obtained from the same DNS pairs as in (*a*); ● ● ● (magenta), derivative of (3.5).

pairs (i,j) is obtained in the core of the channel, leads to $\kappa = 0.42$. The resulting good collapse in the region $0.4 \lesssim Y \leq 1$ of the $U_{out,1}^+(Y)$, obtained from different pairs, is shown in figure 4(*a*), together with the fit

$$\hat{U}_{out,1}^+ = -210 - 130\cos(\pi Y) \sim -340 + O(Y^2) \quad \text{for} \quad Y \to 0, \qquad (3.5)$$

where the reader is reminded that analytical fits are designated by hats, while quantities derived from DNS profiles are left without.

As it turns out, the optimal $\kappa = 0.42$ is rather sharply defined, as seen from the divergence of the $U_{out,1}^+(Y)$ profiles for $\kappa = 0.41$, obtained from the same profile pairs and included in figure 4(*a*) in grey. The confidence in the fit (3.5) is reinforced by the good match in figure 4(*b*) between the derivative of the fit (3.5) and the derivatives $\mathrm{d}U_{out,1}^+/\mathrm{d}Y$ obtained from the same profile pairs as in figure 4(*a*), with a scheme analogous to (3.3) that requires no knowledge of κ.

Since the determination of $U_{out,1}^+(Y)$ is a key step of the present analysis, which tests the limits of present DNS, it is useful to compare with the parameter-free method (ii), based on three DNS profiles and outlined in § 3.1. The resulting $U_{out,1}^+(Y)$ is shown in figure 5(*a*) for four profile triplets and the corresponding κ values are shown in panel (*b*). What is striking in this figure, are the surprisingly good results for the two triplets involving only profiles from table 1. The results for κ in particular, which deviate on the centreline by less than ± 0.003 from 0.42, are outstanding. In contrast, the results from the two triplets including a profile of table 2 are rather useless for the present purpose. They have been included to show why the present methodology fails with a number of DNS profiles: as seen in figure 5, the two 'bad' triplets yield results consistent with the two 'good' ones up to around $Y \approx 0.2$, where they are of no interest for the outer expansion, and become erratic towards the centreline. This suggests an imbalance of computational effort between near-wall and core regions, which has been recognized and corrected by the Texas group
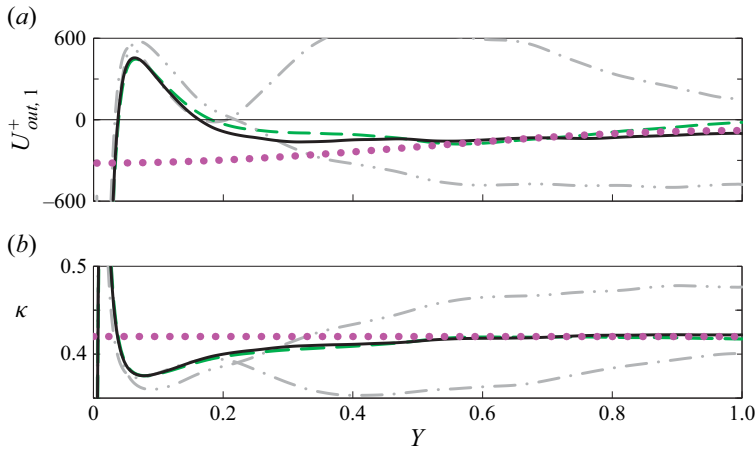
Figure 5. (*a*) Higher-order term $U_{out,1}^+(Y)$ of the outer expansion obtained from three DNS of table 1: —, (#1,#2,#3); - - - (green), (#1,#2,#4). Results involving one DNS of table 2: $-\cdot-$ (grey), (#2,#3,#6); $-\cdot\cdot-$ (grey), (#2,#3,#5); • • • (magenta), fit by (3.5). (*b*) κ from the same triplets as in panel (*a*); • • • (magenta), $\kappa = 0.42$.

Profile	Re_τ	Colour in figures	Reference
#5	4179	■ (brick red)	Lozano-Durán & Jiménez (2014)
#6	3000	■ (red)	Thais, Mompean & Gatski (2013)

Table 2. Channel DNS profiles used to validate the composite fit (3.17).

during the computations for Lee & Moser (2015) (private communication of R. Moser and M.K. Lee).

To complete the outer expansion, the leading-order term of $U_{out}^+(Y)$ is split into several contributions

$$U_{out}^+(Y) = \left\{ \frac{1}{0.42} \ln[Re_\tau Y(2-Y)] + C + W_0(Y) \right\} + \frac{1}{Re_\tau} U_{out,1}^+ + \cdots, \quad (3.6)$$

where all the terms, including the outer log term, satisfy the channel symmetry $U^+(Y) = U^+(2-Y)$. This requirement is rarely implemented in the literature, where the original decomposition of Coles (1956) into simple logarithm and 'wake' dominates. The only unknowns left in the outer expansion (3.6) are the constant C and the 'wake function' $W_0(Y)$ (note that W_0 is different from Coles' wake function because of the symmetrized log term). Specifying $W_0(Y = 1) = 0$ in (3.6) leads to the 2-term expansion of the centreline velocity

$$\hat{U}_{cl}^+ = \left\{ \frac{1}{0.42} \ln(Re_\tau) + 6.22 \right\} - \frac{80}{Re_\tau} + O(Re_\tau^{-2}), \quad (3.7)$$

with the optimal $C = 6.22$. Equation (3.7) is seen in figure 6 to reproduce the reference DNS data of table 1 with an error of less than 0.2 %, which is marginally better than the leading-order fit by Monkewitz (2017).
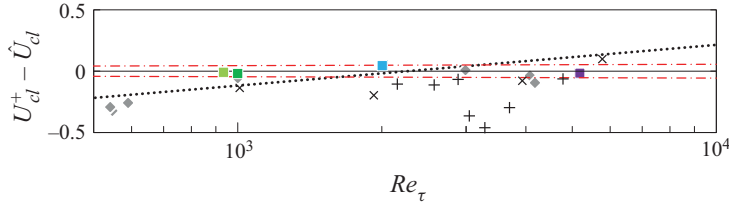
Figure 6. Various channel/duct centreline velocities minus $\hat{U}_{cl}^+$ ((3.7)) versus Re_τ. ■ (purple) ■ (sky blue) ■ (green) ■ (spring green), DNS of table 1; ♦ (grey), other DNS used in Monkewitz (2017); ×, Schultz & Flack (2013); +, Zanoun, Durst & Nagib (2003). $\cdot - \cdot$ (red), $\pm 0.2\%$ of $\hat{U}_{cl}^+$. $\cdots$, slope corresponding to the Musker $\kappa_M = 0.398$ ((3.16)).
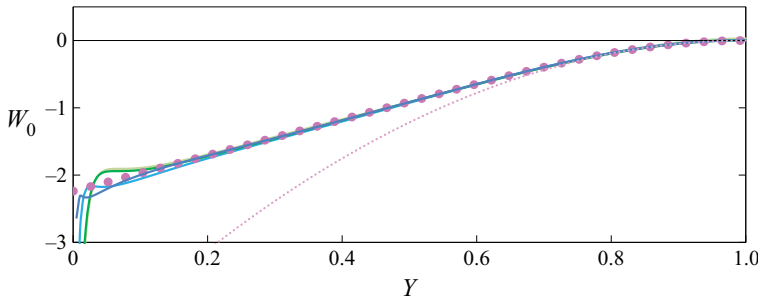
Figure 7. Value of $W_0(Y)$ obtained from (3.6), with $U_{out}^+(Y)$ approximated by the four DNS profiles of table 1 (colours as in the table). ●●● (magenta), fit by (3.8); $\cdots$ (magenta), leading term -4.87 $(1 - Y)^2$ of Taylor expansion around $Y = 1$.

Finally, W_0 is obtained from (3.6) by using the fit (3.5) for $U_{out,1}^+$ and identifying the total velocity U_{out}^+ with U_{DNS}^+ in the outer region. The resulting $W_0(Y)$ is shown in figure 7, together with its fit

$$
\left.
\begin{aligned}
\frac{d\hat{W}_0}{dY} &= 2.66 \tanh\left\{3.66\frac{1-Y}{[Y(2-Y)]^{2.5}}\right\}, \\
\hat{W}_0 &= -\int_Y^1 [d\hat{W}_0/dY](Y')\, dY' \sim -2.24 + 2.66Y + O(Y^2) \quad \text{for } Y \to 0,
\end{aligned}
\right\}
\tag{3.8}
$$

which is necessarily rather elaborate to avoid compromising the determination of the inner expansion in § 3.3. Note that the collapse of W_0 from different DNS in figure 7 justifies the functional form of $U_{out,0}^+$ in (3.6).

The two fits $\hat{U}_{out,1}^+$ and $\hat{W}_0$ complete the formal description of the 2-term outer expansion (3.6) of U^+. For the matching to the inner expansion, to be developed in § 3.3, the limiting behaviour of $\hat{U}_{out}^+$ for $Y \to 0$ is required. After expanding the logarithm in (3.6) and using the fits (3.5) and (3.8), one obtains for $Y \ll 1$

$$
\hat{U}_{out}^+(Y \ll 1) \sim \frac{1}{0.42}\ln(Re_\tau Y) + 5.63 + 1.47Y - \frac{340}{Re_\tau} + O(Re_\tau^{-2}),
\tag{3.9}
$$

where the log-law constant $B = 5.63$ is the result of $C = 6.22$ minus 2.24 ((3.8)) plus $\ln(2)/0.42$ from the Taylor expansion of the logarithm in (3.6).
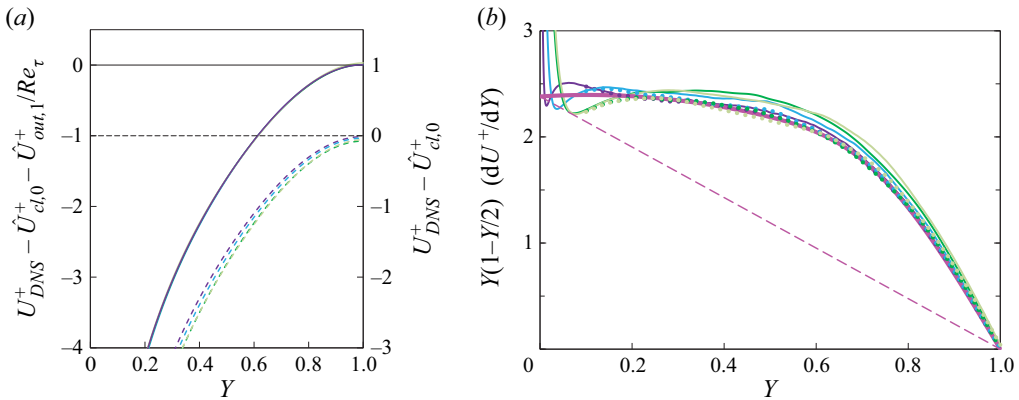
910 A45-12

Figure 8. (*a*) The effect of subtracting the fit $\hat{U}^+_{out,1}$ ((3.5)) from the four DNS profiles of table 1. (*b*) Solid lines, outer indicator function $Y(1 - Y/2)(dU^+_{DNS}/dY)$ versus Y for the three highest Re_τ; corresponding ●●●, DNS minus first-order fit $Y(1 - Y/2)(d\hat{U}^+_{out,1}/dY)Re_\tau^{-1}$ ((3.5)); — (magenta), leading-order fit $Y(1 - Y/2)(d\hat{U}^+_{out,0}/dY)$ ((3.6) and (3.8)); - - - (magenta), $Y(1 - Y/2)$ times derivative of logarithm in (3.6).

The terms of (3.9) will appear in the common part, only if they have a counterpart in the limit $y^+ \gg 1$ of the inner expansion. As will be seen in § 3.3, this is the case for all the terms in (3.9).

Before moving on to the inner expansion, it is worthwhile to document in figure 8 the significant improvement in the description of the outer velocity profile, brought about by the $O(Re_\tau^{-1})$ correction (3.5). Panel (*a*) documents the improved collapse of the four profiles of table 1 in the central part of the channel. Panel (*b*) is a variation of figure 7(*a*) of Jiménez & Moser (2007), showing the 'outer indicator function' with the proper symmetry about the centreline. It clearly demonstrates the improved profile collapse brought about in the central part of the channel by subtracting the outer $O(Re_\tau^{-1})$ contributions associated with $\hat{U}^+_{out,1}$ ((3.5)) from the DNS data. The discussion of the indicator function near the wall, obtained by subtracting the inner $O(Re_\tau^{-1})$ contributions from DNS, is deferred to figure 12.

3.3. *The inner expansion $U^+_{in}(y^+)$ and the final matching*

Starting again with the order $O(Re_\tau^{-1})$, the first order of the inner expansion $U^+_{in,1}(y^+)$ is determined with (3.3). Although at the limit of DNS uncertainty, different pairs of the profiles in table 1 yield reasonably consistent $U^+_{in,1}$, seen in figure 9 to have three distinct features:

   (i) An initial negative excursion near the origin due to the pressure gradient, which produces the exact quadratic term $-(\beta/2)(y^+)^2$ in the Taylor expansion of U^+ about the wall. This minute negative part is correctly reproduced by two of the four DNS pairs.
  (ii) A first-order 'hump' very similar to the hump proposed by Nagib & Chauhan (2008) to improve the Musker profile (see appendix A and (A7)), except that its height diminishes as Re_τ^{-1}.
 (iii) A final approach to the linear function $1.47y^+ - 340$ which matches the linear part of $\hat{U}^+_{out}(Y \ll 1)$ ((3.9)).
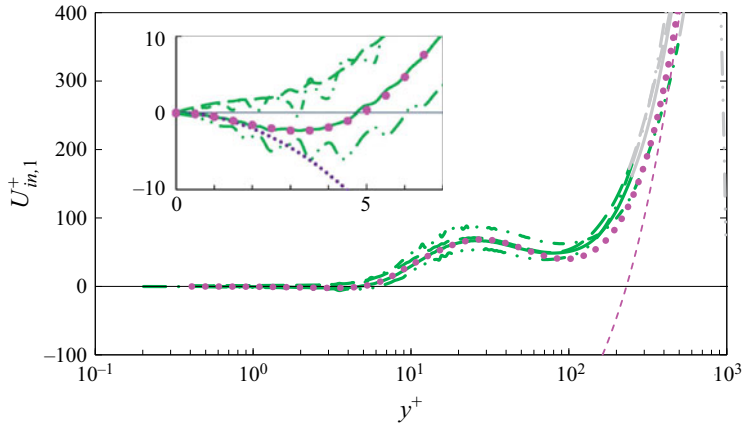
Figure 9. First-order term $U_{in,1}^+(y^+)$, obtained from differences (3.3) of U^+-profiles in table 1. Profile pairs and line styles as in figure 5(a) (green lines up to $Y = 0.25$ for the lower Re_τ of the pair, grey lines beyond). ● ● ● (magenta), complete fit $\hat{U}_{in,1}^+$ ((3.10)); - - - (magenta), linear function $1.47y^+ - 340$ matching the linear part of $\hat{U}_{out}^+(Y \ll 1)$ ((3.9)). Inset: blowup of the origin with $\cdots$ (violet), $-(1/2)(y^+)^2$.

These three distinct features of the first-order inner velocity are fitted by the three terms of

$$\hat{U}_{in,1}^+ = -\tfrac{1}{2}(y^+)^2 \exp[-0.004(y^+)^3] + \hat{H}_{NC}(y^+; 67, 0.75, 27)$$
$$+ 490.5 \ln \cosh[2.99610^{-3}y^+] \sim 1.47y^+ - 340 \quad \text{for} \quad y^+ \to \infty, \quad (3.10)$$

with $\hat{H}_{NC}$ the 'hump' function (A7). As required, the large y^+ limit of $\hat{U}_{in,1}^+/Re_\tau$ matches the corresponding terms in the small Y expansion (3.9) of $\hat{U}_{out}^+$. Hence, the common part of the 2-term inner and outer expansions is

$$\hat{U}_{cp}^+(Y) = \left\{ \frac{1}{0.42} \ln(Re_\tau Y) + 5.63 + 1.47Y \right\} - \frac{340}{Re_\tau} + O(Re_\tau^{-2}), \quad (3.11)$$

or equivalently

$$\hat{U}_{cp}^+(y^+) = \left\{ \frac{1}{0.42} \ln(y+) + 5.63 \right\} + \frac{1}{Re_\tau}\{1.47y^+ - 340\} + O(Re_\tau^{-2}). \quad (3.12)$$

The leading term $U_{in,0}^+$ of the inner expansion is now finally obtained by identifying the 2-term composite expansion with the DNS profile

$$U_{DNS}^+ \cong U_{in,0}^+ + \hat{U}_{out,0}^+ - \hat{U}_{cp,0}^+(y^+) + \frac{1}{Re_\tau}\left\{ \hat{U}_{in,1}^+ + \hat{U}_{out,1}^+ - \hat{U}_{cp,1}^+(y^+) \right\}, \quad (3.13)$$

with the common part expressed in terms of y^+, i.e. split into leading- and first-order parts according to (3.12). The resulting $U_{in,0}^+$ minus the leading-order common part is shown on the left axis of figure 10. For comparison, the same quantity, obtained without the $O(Re_\tau^{-1})$ terms in (3.13), is plotted on the right axis and the striking improvement brought about by taking $O(Re_\tau^{-1})$ terms into account is evident. This improvement also reveals a clean logarithmic region of $U_{in,0}^+$ beyond $y^+ \approx 150$, where the Musker fit has already reached its design logarithmic asymptote with $\kappa_M = 0.398$ and $B_M = 4.717$. This first logarithmic
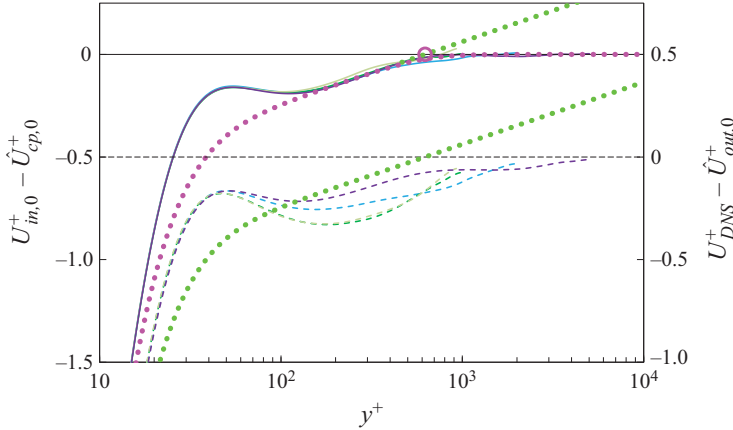
910 A45-14

Figure 10. Left axis and solid lines: leading-order inner velocity $U_{in,0}^+$ minus $\hat{U}_{cp,0}^+(y^+)$ obtained from (3.13) and (3.12) for the four profiles of table 1. Right axis and broken lines: leading-order inner velocity minus common part, equal to $U_{DNS}^+ - \hat{U}_{out,0}^+$, determined without the $O(Re_\tau^{-1})$ terms in (3.13). $\cdots$ (lime green), improved Musker profile $\hat{U}_{mM}^+$ ((A6)) without 'hump', for $\kappa_M = 0.398$ and $B_M = 4.784$, minus $\hat{U}_{cp,0}^+(y^+)$ ((3.12)); $\cdots$ (magenta), $\hat{U}_{mM}^+ - \hat{U}_{cp,0}^+(y^+) - \hat{\Delta}_{\log,Ch}$, including the change in logarithmic slope ((3.14)) at $\bigcirc$ (magenta), the breakpoint $y_{break}^+ = 624$.

region ends at a breakpoint $y_{break}^+ = 624$ (the magenta circle in figure 10), where $U_{in,0}^+$ switches to the true leading-order overlap log law $(1/0.42)\ln(y^+) + 5.63$ of (3.12).

This change of logarithmic slope at $y_{break}^+ = 624$ is well fitted by the function

$$\hat{\Delta}_{\log,Ch}(y^+) = \frac{1}{4}\left[\frac{1}{0.398} - \frac{1}{0.42}\right]\ln\left[1 + \left(\frac{y^+}{624}\right)^4\right], \quad (3.14)$$

already used by Monkewitz (2017).

The last term of the 2-term composite expansion of U^+ to be fitted is $U_{in,0}^+$. This is achieved in two steps. First, the modified Musker profile ((A6)) with $\kappa_M = 0.398$ and $B_M = 4.784$ is subtracted, and the changeover to the true log law $\hat{\Delta}_{\log,ch}^+$ ((3.14)) is added. The result is shown in figure 11(a) which reveals the leading-order hump, seen to be similar to the one discussed by Nagib & Chauhan (2008). To maintain the highest possible fidelity of the fits, the hump of figure 11(a) is described by the modified Hump function

$$\hat{H}_{mNC}(y^+) = \hat{H}_{NC}(y^+; 0.313, 1.3, 33) - 4 \times 10^{-5}(y^+)^4 \exp\left[-(0.12y^+)^{2.5}\right], \quad (3.15)$$

with the function $\hat{H}_{NC}$ given by (A7).

Putting (A6), (3.14) and (3.15) together, the complete fit of $U_{in,0}^+$ is obtained as

$$\hat{U}_{in,0}^+ = \hat{U}_{mM}^+(y^+; 0.398, 4.784) - \hat{\Delta}_{\log,Ch} + \hat{H}_{mNC}. \quad (3.16)$$

At this point, all the terms of the composite expansion have been fitted, and the complete 2-term composite fit

$$\hat{U}_{comp}^+ \cong \hat{U}_{in,0}^+ + \hat{U}_{out,0}^+ - \hat{U}_{cp,0}^+(y^+) + \frac{1}{Re_\tau}\left\{\hat{U}_{in,1}^+ + \hat{U}_{out,1}^+ - \hat{U}_{cp,1}^+(y^+)\right\}, \quad (3.17)$$
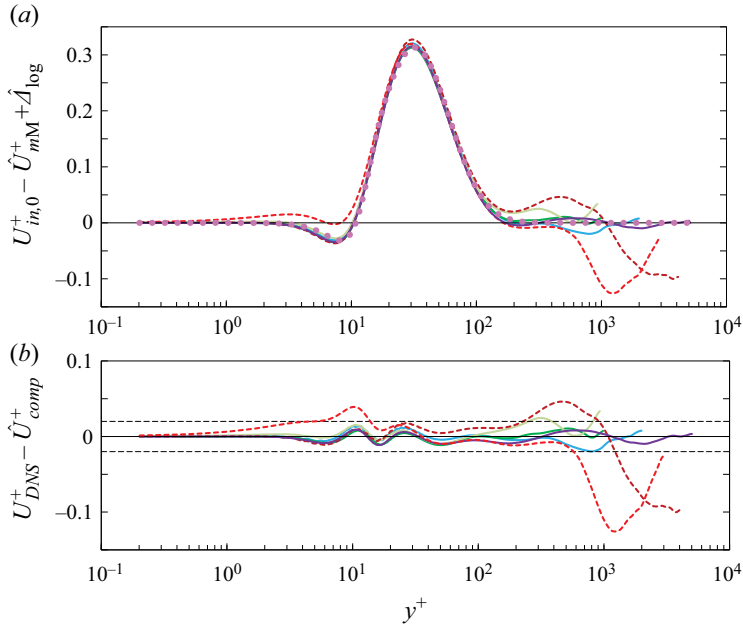
910 A45-15

Figure 11. (*a*) Value of $U_{in,0}^+ - \hat{U}_{mM}^+ + \hat{\Delta}_{\log,Ch}$ ((A6) and (3.14)) for the four profiles of table 1 (colour scheme in table); ● ● ● (magenta), fit by (3.10) (*b*) DNS profiles U_{DNS}^+ minus complete composite fit $\hat{U}_{comp}^+$ up to and including $O(Re_\tau^{-1})$ terms; horizontal dashed lines indicate ± 0.02 from the composite fit. (*a,b*): - - -, validation cases of table 2 (colour scheme of table).

can now be compared to the four DNS profiles of table 1. The result is shown in figure 11(*b*) which demonstrates an unprecedented collapse of all the four DNS profiles onto the composite profile $\hat{U}_{comp}^+$, with absolute deviations of less than ± 0.02.

This is also the moment to validate the new 2-term composite MVP fit ((3.17)), obtained as the average from different combinations of the four DNS in table 1, by comparing to the two profiles from independent sources in table 2. As seen in figure 11, the validation profiles are within the band of variations between the four 'Master' profiles up to $y^+ \approx 200$, but show deviations of the order of 0.1 in the outer part. While this represents less than 0.5 % of the local U^+, it prevented the use of these profiles for the determination of $U_{out,1}^+$ (see also figure 5).

As the implications of pushing the asymptotic expansion of U^+ to order $O(Re_\tau^{-1})$ and of the excellent data collapse in figure 11 may not be obvious, the indicator function $\Xi^+ = y^+(\mathrm{d}U^+/\mathrm{d}y^+)$, commonly used to locate logarithmic regions, is examined next. Since the overlap log-law results from an asymptotic argument, it must correspond to a region where the leading-order indicator function is constant. With the present results it is, for the first time, possible to subtract the first-order contribution of $O(Re_\tau^{-1})$ from the full indicator profiles, as shown in figure 12. The salient features of this figure are:

(i) The Ξ_{DNS}^+, obtained directly from DNS profiles, as well as the composite $\hat{\Xi}_{comp}^+$ at higher Re_τ are substantially different from the leading-order fit of the inner indicator function $\hat{\Xi}_{in,0}^+$, obtained from (3.16). Here, and in the following, Ξ^+ with a subscript indicates which term of the asymptotic expansion of U^+ is used. The large deviation of Ξ_{DNS}^+ from the leading order is principally due to the third part of

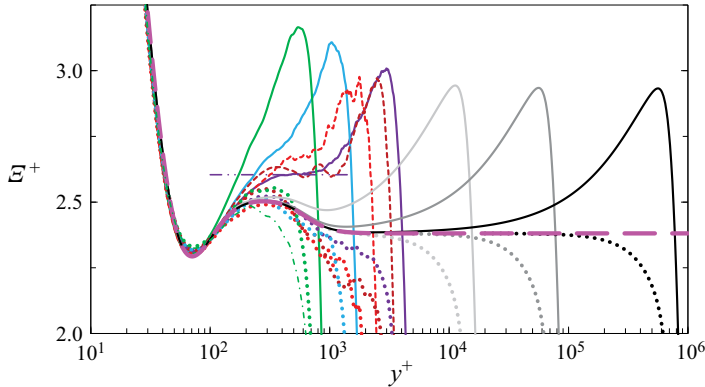Figure 12. Solid lines, channel indicator function Ξ_{DNS}^+ versus y^+ for the three highest Re_τ of table 1 plus three profiles obtained from the 2-term composite expansion (3.17) for $Re_\tau = 2 \times 10^4$, 10^5 and 10^6; short dashes - - -, Ξ_{DNS}^+ of validation profiles in table 2 (colours as in table); ● ● ●, corresponding $\Xi_{DNS}^+ - \hat{\Xi}_{in,1}^+$; $- \cdot -$ (spring green), $\Xi_{DNS}^+ - \hat{\Xi}_{in,1}^+ - \hat{\Xi}_{out,1}^+$ for profile #3 of table 1. $- - -$ (magenta), leading-order inner fit $\hat{\Xi}_{in,0}^+$ (obtained from (3.16)); $- \cdot \cdot -$ (purple), transitory plateau $1/0.384$ in Ξ_{DNS}^+ for profile #1 of table 1.

$\hat{U}_{in,1}^+$ ((3.10)), which becomes the linear term $1.47y^+/Re_\tau$ in the common part (3.12). The contribution of the outer $\hat{\Xi}_{out,1}^+$ ((3.5)) is shown in figure 12 only for $Re_\tau = 10^3$ (profile #3 of table 1), as it becomes negligible in the overlap region for $Re_\tau \gtrsim 4000$.

(ii) From the above it is obvious, that the emergent horizontal tangent of Ξ_{DNS}^+ in profile #1 of table 1 and #5 of table 2 is a transient feature for $Re_\tau \approx 5000$, not related to the true overlap plateau of the leading-order indicator function at $1/0.42$.

(iii) The full indicator function Ξ_{DNS}^+ only reveals the true overlap plateau, i.e. the clean overlap log law with $\kappa = 0.42$, well beyond a Re_τ of 10^5. For $Re_\tau = 10^6$ this plateau extends from $y^+ = 10^3$ to 10^4, or $Y = 10^{-3}$ to 10^{-2}, with the intermediate variable $y^+ Re_\tau^{-1/2} = O(1)$, as 'in the textbook'. This means, that at the highest DNS Re_τ of 5186 it is not possible to obtain the true overlap κ from the indicator function.

(iv) Figure 12 finally shows, that subtracting the fit $\hat{\Xi}_{in,1}^+$ for the first-order inner indicator function from Ξ_{DNS}^+ dramatically improves the situation: It produces a good collapse of all the data derived from DNS onto the leading order $\Xi_{DNS}^+ - \hat{\Xi}_{in,1}^+$ and suggests that, by subtracting $\hat{\Xi}_{in,1}^+$, the true overlap log law could be identified already at $Re_\tau \cong 2 \times 10^4$.

It is also worthwhile to compare the Reynolds stress from DNS to the fit obtained from the momentum equation and the derivative of the 2-term composite expansion (3.17). The result is shown in figure 13 for four Re_τ. For $Re_\tau = 5186$ the composite expansion is seen to match the DNS #1 of table 1 within plotting accuracy, as expected from the quality of the fit for U^+, shown in figure 11(b). Also included in figure 13 are the locations and values of the Reynolds stress maxima. As the maximum results from a balance between derivatives of inner and outer U^+, its location scales on the intermediate variable $\eta = y^+ Re_\tau^{-1/2} = YRe_\tau^{1/2}$, as recognized by Sreenivasan & Sahay (1997). Hence, for sufficiently high Re_τ, the Reynolds stress maximum must be located
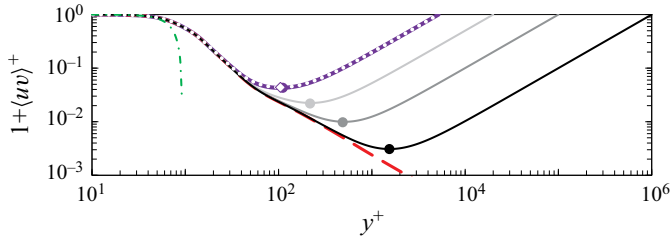
Figure 13. Solid lines, $1 + \langle uv \rangle^+$ obtained from the momentum equation and the 2-term composite expansion of $\hat{U}^+$, for $Re_\tau = 5186$, 2×10^4, 10^5 and 10^6; - - - (red), $Re_\tau = \infty$; small white ○, 1 minus computed Reynolds stress from DNS #1 in table 1. ●, value and location of maximum Reynolds stress ((3.18a,b)) for the four Re_τ, with $\kappa = 0.42$; white ◇, maximum Reynolds stress from DNS #1; $- \cdot -$ (green), Taylor expansion $1 - 0.00125(y^+)^3 + \cdots$ around $y^+ = 0$.

within the logarithmic common part of inner and outer expansions

$$y^+_{maxRS} = \left(\frac{Re_\tau}{\kappa} \right)^{1/2} + O(Re_\tau^{-1/2}), \quad 1 + \langle uv \rangle^+_{max} = \frac{2}{(\kappa Re_\tau)^{1/2}} + O(Re_\tau^{-1}). \quad (3.18a,b)$$

This leading-order result, stated already by Lee & Moser (2015), with $\kappa = 0.42$ is seen in figure 13 to closely match even the DNS for $Re_\tau = 5186$, despite y^+_{maxRS} being still well below the start of the overlap layer at $y^+_{break} = 624$. Equation (3.18a,b) with $\kappa = 0.42$ yields $1 + \langle uv \rangle^+_{max} = 3.09/Re_\tau^{1/2}$, which is within 0.3 % of the correlation of Sreenivasan & Sahay, but the location $y^+_{maxRS} = 1.54 Re_\tau^{1/2}$ is slightly below the range of $1.6 - 2Re_\tau^{1/2}$ in their figure 2. Note, however, that Sreenivasan & Sahay (1997) implicitly assumed the same κ for channel and pipe, which is not justified in view of the present findings.

Finally, it is interesting to note that the leading term $0.00125(y^+)^3$ of the Taylor expansion of the fitted Reynolds stress around $y^+ = 0$ is, within the uncertainty, identical to $0.00127(y^+)^3$ estimated by Monkewitz & Nagib (2015) from DNS of ZPG TBLs.

In conclusion, this analysis has, for the first time, uncovered the true asymptotic channel MVP, which is, at the Re_τ of current DNS, hidden 'under' the inner and outer finite Reynolds number corrections. In particular, it has shown, that there is a statistically significant difference between the near-wall Musker κ_M and the overlap κ (see figure 12). In other words, the asymptotic structures of channel and Superpipe MVPs are similar, as seen in figure 14.

4. Evidence for the hypothesis (2.1) in Couette flow and review of pipe DNS

4.1. *Couette flow*

The main test of the hypothesis (2.1) consists of the demonstration, that in Couette flow the logarithmic slope of U^+ increases at y^+_{break}. In terms of an 'eddy' model, this increase of logarithmic slope in the region $y^+ \geq y^+_{break}$ is brought about by eddies, which originate from the opposite wall, evolve and weaken progressively, and finally stop contributing to the mean shear at y^+_{break}. It would be desirable to construct inner and outer asymptotic expansions to order $O(Re_\tau^{-1})$ analogous to those for the channel in § 3. However, as seen in figure 15, the available DNS are limited to $Re_\tau \lesssim 10^3$ and there are doubts on whether the turbulence is fully developed below Re_τ of 500. Furthermore, several of the authors cited
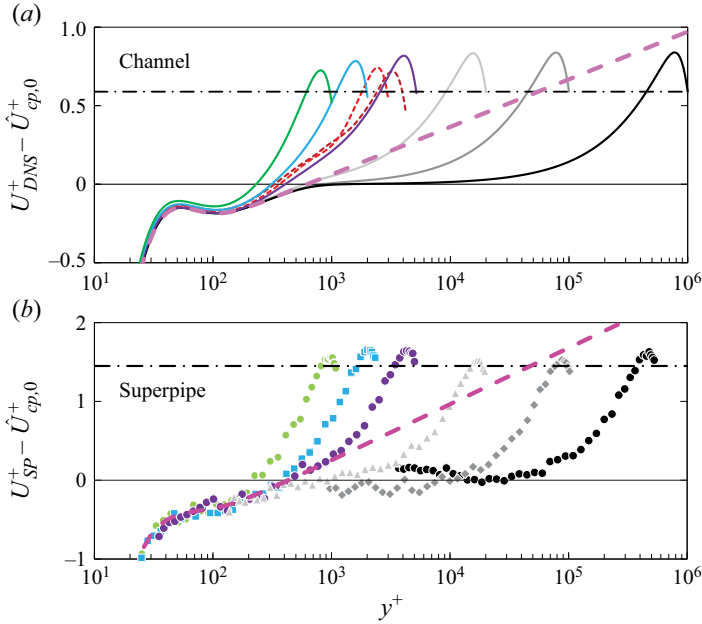
910 A45-18

Figure 14. (*a*) Channel mean velocity profiles minus the leading-order common part $\hat{U}_{cp,0}^+ = (1/0.42)\ln(y^+) + 5.63$ ((3.12)). DNS profiles from tables 1 and 2 plus composite profiles for $Re_\tau = 2 \times 10^4, 10^5$ and 10^6 ((3.17)), with same colour scheme as in figure 12. - - - (magenta), modified Musker profile $\hat{U}_{mM}^+(y^+; 0.398, 4.78)$ ((A6)) plus 'hump' $\hat{H}_{mNC}$ ((3.15)) minus $\hat{U}_{cp,0}^+$. $- \cdot -$, $\hat{U}_{cl,0}^+ - \hat{U}_{cp,0}^+ = 0.59$. (*b*) Analogous graph for the Superpipe profiles of Zagarola & Smits (1998) at comparable Re_τ values of $1.09, 2.35, 5.02, 19.7, 102, 529 \times 10^3$ minus the common part $\hat{U}_{cp,0}^+ = (1/0.436)\ln(y^+) + 6.20$. - - - (magenta), Musker profile $\hat{U}_M^+(y^+; 0.384, 4.26) + \hat{H}_{NC}(y^+; 0.351, 1, 30)$ ((A1) and (A7)) minus $\hat{U}_{cp,0}^+$. Change of log slope (intersection of Musker asymptote and $\hat{U}_{cp,0}^+$) at $y_{break}^+ = 450$. $- \cdot -$, $\hat{U}_{cl}^+ - \hat{U}_{cp}^+ = 1.45$, corresponding to $\hat{U}_{cl}^+$ of figure 1(*b*).
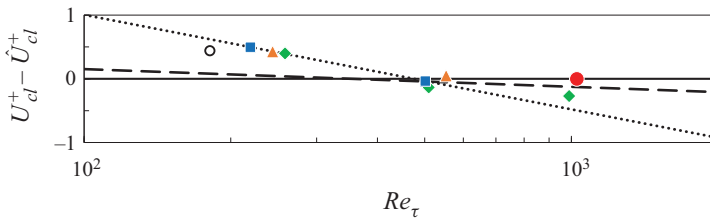

Figure 15. Various Couette centreline velocities minus $\hat{U}_{cl}^+$ ((4.1)) versus Re_τ from different DNS. ∘, Tsukahara, Kawamura & Shingai (2006); ■ (Blue), Lee & Moser (2018); ▲ (orange), Avsarkisov *et al.* (2014); ♦ (green), Pirozzoli, Bernardini & Orlandi (2014); • (red), Kraheberger *et al.* (2018). - - -, $(1/0.384)\ln(Re_\tau) + 3.75$ minus (4.1); $\cdots$, $(1/0.481)\ln(Re_\tau) + 7.01$ minus (4.1).

in the caption of figure 15 report, that even the MVP is sensitive to both the streamwise and spanwise sizes of the computational box.

Therefore, only the most recent profile of Kraheberger *et al.* (2018) for the highest $Re_\tau = 1026$, obtained with state of the art numerical methods, is analysed here. This, of course, limits the analysis to the leading order of inner and outer expansions and leaves some uncertainty about the coefficients of the expansions.

To start the analysis, the centreline κ and C are determined from the data points of Lee & Moser (2018) at $Re_\tau = 501$ and Kraheberger *et al.* (2018) at $Re_\tau = 1026$ in figure 15:

$$\hat{U}_{cl}^+ = \frac{1}{0.367} \ln(Re_\tau) + 3.04. \tag{4.1}$$

Analogous to (3.6) for the channel, except for the opposite symmetry of the logarithm about the centreline, the leading-order outer velocity is described by

$$\hat{U}_{out}^+(Y) = \frac{1}{0.367} \ln\left[\frac{Re_\tau Y}{2 - Y}\right] + 3.04 + W_0(Y) \quad \text{with} \quad W_0(Y) = 2.15 \cos\left(\frac{\pi}{2} Y\right), \tag{4.2}$$

$$\hat{U}_{out}^+(Y \ll 1) \sim \frac{1}{0.367} \ln(Re_\tau Y) + 3.30 + 1.36 Y + O(Y)^2. \tag{4.3}$$

Since the linear term in the small-Y limit (4.3) translates in the inner expansion to a first-order term, not considered here, the common part consists of just the log law in (4.3):

$$\hat{U}_{cp}^+ = \frac{1}{0.367} \ln(y^+) + 3.30. \tag{4.4}$$

The simple wake function $W_0(Y)$ of (4.2) is seen in panel (*a*) of figure 16 to provide an excellent fit to the DNS for $Y \gtrsim 0.4$, which is all that can be expected at this low Reynolds number. Panel (*b*) of figure 16 shows the same $U_{DNS}^+(y^+)$ minus the outer fit $\hat{U}_{out}^+$ (equation (4.2)), which is equal to $\hat{U}_{in}^+ - \hat{U}_{cp}^+$, up to terms of order $O(Re_\tau^{-1})$. Fitting $\hat{U}_{in}^+$ with the modified Musker profile plus hump, $\hat{U}_{mM}^+(y^+; 0.367, 3.30) + \hat{H}_{NC}(y^+; 0.38, 1, 34)$ ((A6) and (A7) with the overlap parameters of (4.4)), is seen in figure 16(*b*) to be obviously inadequate. A proper fit of U_{in}^+ is only possible with $\kappa_M = 0.40$, requiring a change of logarithmic slope at $y_{break}^+ = 379$, described by the function

$$\hat{\Delta}_{\log,Cou}(y^+) = \frac{1}{4}\left[\frac{1}{0.40} - \frac{1}{0.367}\right] \ln\left[1 + \left(\frac{y^+}{379}\right)^4\right], \tag{4.5}$$

similar to $\hat{\Delta}_{\log,Ch}$ of (3.14).

Hence, the leading order of the inner expansion for the mean velocity in Couette flow is

$$\hat{U}_{in}^+ = \hat{U}_{mM}^+(y^+; 0.40, 4.64) + \hat{H}_{NC}(y^+; 0.38, 1, 34) - \hat{\Delta}_{\log,Cou}(y^+), \tag{4.6}$$

with the different terms given by (A6), (A7) and (4.5), respectively. The final composite profile is obtained by combining equations (4.2), (4.4) and (4.6). The result is seen in figure 16(*c*) to provide an excellent description of the DNS profile of Kraheberger *et al.* (2018), except for the 'wiggle' between $y^+ \approx 2$ and 70, which is due to the simple hump model of (A7). No attempt has been made to improve the hump fit as for the channel, because the central point, the demonstration of a switch from a lower (1/0.40) to a higher (1/0.367) logarithmic slope at $y_{break}^+ \approx 400$, is not affected.

4.2. *The prospects of extracting asymptotic expansions from pipe DNS*

Of the three flows considered in this paper, pipe flow is by far the one of largest practical interest and it would therefore be highly desirable to develop a complete asymptotic description of its MVP from DNS, analogous to the one for the channel in § 3.
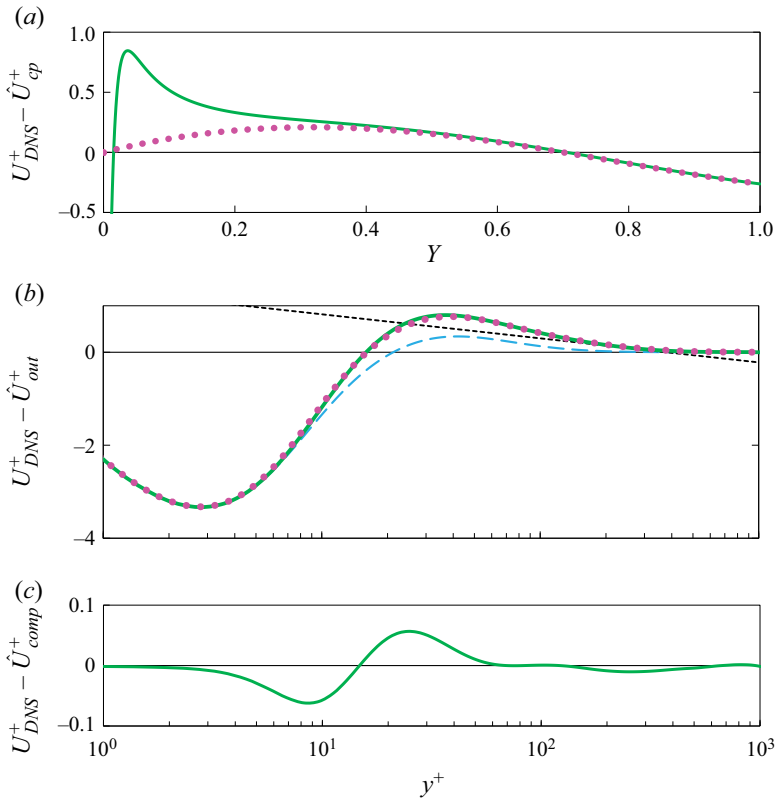
Figure 16. (*a*) — (green), Difference between the U^+-profile of Kraheberger *et al.* (2018) for $Re_\tau = 1026$ and $\hat{U}^+_{cp}$ ((4.4)); • • • (magenta), outer fit $\hat{U}^+_{out}(Y)$ ((4.2)) minus $\hat{U}^+_{cp}$ ((4.4)). (*b*) — (green), $U^+_{DNS}(y^+)$ minus the outer fit $\hat{U}^+_{out}$ ((4.2)); - - - (aquamarine), $\hat{U}^+_{mM}(y^+; 0.367, 3.30) + \hat{H}_{NC}(y^+; 0.38, 1, 34)$ ((A6) and (A7)); • • • (magenta), $\hat{U}^+_{in} - \hat{U}^+_{cp}$ ((4.6) and (4.4)); - - -, asymptote of $\hat{U}^+_{mM}(y^+; 0.40, 4.64)$. (*c*) — (green), $U^+_{DNS}(y^+)$ minus the composite fit $\hat{U}^+_{in} + \hat{U}^+_{out} - \hat{U}^+_{cp}$.

However, the three DNS data points, included as red squares in figure 1, do not even provide a consistent fit for the centreline velocity. Looking at the lines $\pm(10^3/Re_\tau)$, added to the figure to guide the eye, it appears that the coefficient of Re_τ^{-1} on the centreline must be less than 10^3. However, it is not clear from the present data, whether the higher-order correction is positive, negative or zero – clearly, more high accuracy DNS profiles in the Re_τ range of $10^3 - 5 \times 10^3$ are needed to clarify the situation.

To show the necessary improvements in order to perform an analysis analogous to the one in § 3 for the channel, the DNS profiles minus an example outer logarithmic part

$$W_0(Y) = U^+_{DNS} - \left\{ \tfrac{1}{0.42} \ln[Re_\tau Y(2 - Y)] + 6.84 \right\}, \tag{4.7}$$

are shown in figure 17 for the three pipe DNS of figure 1. Comparing to figure 7, it is obvious that the core region and in particular the handling of the coordinate singularity on the centreline require more attention, before an analysis analogous to § 3 can be envisioned. In conclusion, the extraction of asymptotic expansions from DNS (or experiment) analogous to the channel is not yet feasible, and one is left with considerable uncertainty about κ_M, y^+_{break} and κ for the pipe.
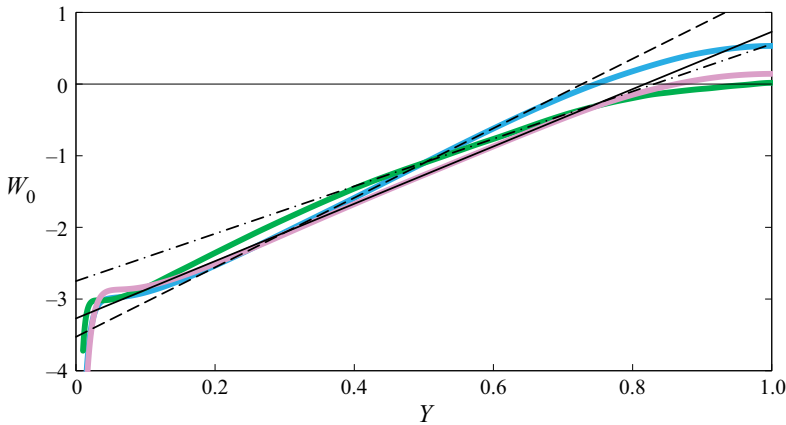
Figure 17. Pipe analogue to figure 7 with W_0 of (4.7), for the three pipe DNS of figure 1: — (lavender), $Re_\tau = 999$, — (aquamarine), $Re_\tau = 1142$ and — (green), $Re_\tau = 2003$. —, - - -, — · —, corresponding tentative linear fits with slopes 4.0, 4.9 and 3.3, respectively.

5. Conclusions

The present investigation, in particular the determination of the 2-term inner and outer asymptotic expansions for the channel, together with the Superpipe data and a detailed analysis of the leading-order asymptotic expansions for a Couette flow DNS, has uncovered a common feature of ducted parallel flows: a change of logarithmic slope of the mean velocity $U^+(y^+)$ at a y^+_{break} of the order $O(10^3)$. According to the hypothesis (2.1), the sign of this slope change depends on the flow symmetry, with a slope decrease in channel and pipe flows and an increase in Couette flow.

The evidence for this phenomenon is strong for channel flow, due to a consistent set of DNS, analysed in § 3, and a rigorous asymptotic analysis, which shows that the log law in the common part of inner and outer mean velocity expansions emerges in the MVP at a much higher Re_τ than previously thought. For Couette flow, the analysis of the DNS profile at the highest available Re_τ supports the hypothesis (2.1), but more DNS for Re_τ in the range $10^3 - 5 \times 10^3$ are needed to confirm the present findings and reduce the parameter uncertainty. For pipe flow, finally, the late start of the logarithmic overlap layer has been firmly established by the Superpipe and CICLoPE experiments, but the available DNS data base does not yet allow an analogous asymptotic analysis to narrow down the estimates of κ_M, κ and y^+_{break}, obtained from the experiments.

The paper concludes with the following list of further observations and open questions:

(i) The analysis of both channel flow in § 3 and Couette flow in § 4.1, found for the logarithmic asymptote of the Musker profile beyond $y^+ \approx 150$ a κ_M of close to 2/5. In the pipe, on the other hand, the different MVP fits require a κ_M closer to the ZPG TBL value of 0.384. So the question, whether κ_M for truly one-dimensional flows is universal or not, will have to wait for more high quality pipe and Couette DNS, which allow the extraction of reliable asymptotic expansions. The reader is reminded here, that the logarithmic asymptote of the Musker profile with slope $1/\kappa_M$ cannot belong to the overlap layer, i.e. the common part of inner and outer expansions, because the outer expansion does not contain the corner and the logarithmic region with slope $1/\kappa_M$ towards the wall.

910 A45-22

(ii) Once the overlap κ values for pipe and Couette flows are finally 'nailed down' with an uncertainty below say ± 0.005, one should be able to answer the question, whether κ is a function of the pressure gradient (see Nagib & Chauhan 2008 for the relation $\kappa(\beta)$ in TBLs), or rather depends on the symmetry S of mean vorticity about the centreline, with $S = -1$ for channel and pipe, and $S = 1$ for Couette flow and/or the duct geometry. In this paper, the change of logarithmic slope $(\kappa^{-1} - \kappa_M^{-1})$ at y_{break}^+ has been determined as -0.13 for channels and $+0.22$ for Couette flow. As the $+0.22$ in § 4.1 may be on the high side (see figure 15), a relation such as $(\kappa^{-1} - \kappa_M^{-1}) \cong 0.13S$ appears possible for channel and Couette flows. However, there is a significant difference between channel and pipe, where $(\kappa^{-1} - \kappa_M^{-1})$ is estimated at $\cong -0.3$, but could be as low as -0.23 based on McKeon *et al.* (2004) – see next point.

(iii) From the present profile analyses, the approximate doubling of $(\kappa^{-1} - \kappa_M^{-1})$ from channel to pipe appears significant and may possibly be explained by taking the hypothesis (2.1) one step further, and also consider a dependence of $(\kappa^{-1} - \kappa_M^{-1})$ on the geometry of the opposite wall. In channel and Couette flows the latter is flat, while its transverse curvature in the pipe could have a focussing effect for perturbations traversing the core. This explanation may be somewhat simplistic and does not take into account probable differences between vortical perturbations in channels and pipes, but cannot be ruled out either.

(iv) The height of the 'hump' above the Musker profile ((A7)) around y^+ of 30 is clearly dependent on Re_τ, as shown in § 3 for channel flow. The maximum overshoot over the logarithmic Musker asymptote $\kappa_M^{-1} \ln(y^+) + B_M$ is approximately $0.19 + (65/Re_\tau)$, which resolves the discrepancies between the height originally proposed by Nagib & Chauhan (2008) and the fits of low Reynolds number data by Luchini (2018).

(v) As discussed in § 1, the linear term λY in the small-Y limit of $U_{out,0}^+$, the leading order of the outer expansion, appears in the common part only if the inner expansion is carried to $O(Re_\tau^{-1})$, i.e. contains a matching term $\lambda y^+/Re_\tau$ in the limit $y^+ \to \infty$. Most recently, Luchini (2017) has claimed that λ is equal to the pressure gradient parameter β, which is equal to 0, 1 and 2 for Couette, channel and pipe flow, respectively. From the present profile analyses, $\lambda = 1.36$ for Couette flow ((4.3)), $\lambda = 1.47$ for channel flow ((3.9)) and $\lambda \in [2.1, 3.7]$ for pipe flow, where these latter values correspond to the range of estimated slopes of the three W_0 profiles in figure 17, minus $(2\kappa)^{-1}$ from the small-Y expansion of $\kappa^{-1} \ln(2 - Y)$ (equation (4.7)). The reason for this discrepancy is exposed in appendix B.

(vi) The sudden decrease of logarithmic slope at $y_{break}^+ \cong 600$, found in § 3.3 for the channel mean velocity U^+, appears also in the profiles of fluctuating pressure $\langle p'p' \rangle^+$ obtained by Panton, Lee & Moser (2017). This is particularly evident for the pressure derived from the $Re_\tau = 5186$ DNS data of Lee & Moser (2015) (profile #1 in table 1): in figure 1(*a*) of Panton *et al.* for the total $\langle p'p' \rangle^+$, the decrease of slope from the interval $y^+ \in [150, 600]$ to $y^+ > 600$ is perceptible, but not very marked. However, in their figure 3 the pressure indicator function for the highest $Re_\tau = 5186$ clearly shows two plateaus with a decrease of logarithmic slope by around 5 % between y^+ of 500 and 10^3. This slope change is also evident in their figure 4(*a*) for the 'rapid pressure'. As noted by Panton *et al.* (2017), the near correspondence between the logarithmic slopes in the $\langle p'p' \rangle^+$ profiles for the channel and the ones obtained in § 3 from the asymptotic analysis of U^+ is unexplained and begs for further research.

(vii) The idea has been advanced by Hultmark *et al.* (2012) and Marusic *et al.* (2013), that the identification of logarithmic regions is facilitated by looking for simultaneous log regions in the MVP and in second order statistics, in particular in $\langle uu \rangle^+$. It has been supported mainly by measurements in the Princeton Superpipe with the NSTAP miniature hot-wires. However, the significant difference between the Pitot and the NSTAP Superpipe MVPs (see Monkewitz (2017), figure 6) have, to this author's knowledge, not been resolved. At lower Re_τ, the second-order statistics do not appear more promising than the MVP to identify log regions, as evidenced by the indicator functions in Lee & Moser (2015, § 3.2) for the channel, where only the spanwise normal stress exhibits a short log region for y^+ between approximately 100 and 300. One may therefore consider the construction of multi-term asymptotic expansions for the second-order statistics, analogous to § 3 for the channel MVP. In order to do this, one has to know the proper asymptotic sequence, but for $\langle uu \rangle^+$, for instance, even the leading term is still being debated. While the 'attached eddy model' leads to an inner peak of $\langle uu \rangle^+$ which increases indefinitely as $\ln(Re_\tau)$, Monkewitz & Nagib (2015) have demonstrated with the help of the complete momentum equation, that this inner peak remains finite in the ZPG TBL (see also the discussion in Monkewitz, Nagib & Boulanger 2017).

(viii) Finally, it might also be interesting to determine the distribution and type of eddies attached to, or originating from the opposite wall, which preserve the logarithmic law in the overlap layer beyond y^+_{break} (for the attached eddy model, see e.g. Marusic & Monty (2019) and references therein).

Author ORCID.
Ⓘ Peter A. Monkewitz http://orcid.org/0000-0003-4279-725X.

Appendix A. The 'Musker' fit for the inner U^+-profile, with additions

The Musker profile (Musker 1979) is obtained by integrating $\mathrm{d}U_M^+/\mathrm{d}y^+ = [\kappa_M S + (y^+)^2][\kappa_M S + (y^+)^2 + \kappa_M(y^+)^3]^{-1}$ analytically, where the subscript M designates parameters used to generate the Musker fit. Note in particular, that κ_M is not necessarily equal to the overlap κ. The two parameters κ_M and S determine the asymptotic behaviour of the Musker profile $\hat{U}_M^+ \sim \ln(y^+)/\kappa_M + B_M$ but, as noted by Nagib & Chauhan (2008), the straightforward integration is prone to numerical near-cancellations. The problem is avoided by recasting the result in the following form:

$$\hat{U}_M^+(y^+; \kappa_M, B_M) = \Gamma_1 \ln\left(1 - \frac{y^+}{g_1}\right) + \frac{\Gamma_2}{2} \ln\left(1 - \frac{g_2 y^+}{g_3} + \frac{(y^+)^2}{g_3}\right)$$
$$+ \frac{2\Gamma_3 + \Gamma_2 g_2}{g_4}\left[\arctan\left(\frac{2y^+ - g_2}{g_4}\right) + \arctan\left(\frac{g_2}{g_4}\right)\right], \quad (A1)$$
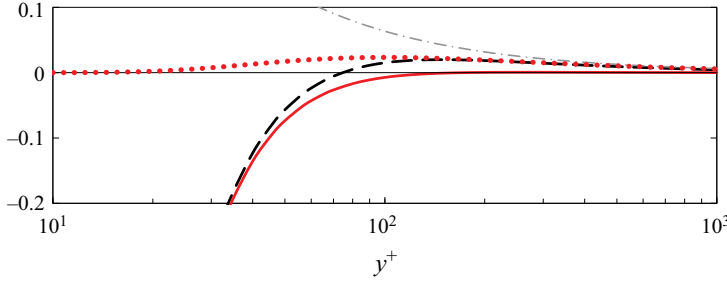
Figure 18. Improvement of the Musker profile (A1): - - -, original $\hat{U}_M^+ - [\kappa_M^{-1} \ln(y^+) + B_M]$ for $\kappa_M = 0.396$ and $B_M = 4.717$ ($S = 905.86$); $- \cdot - \cdot$, asymptotic approach of $\hat{U}_M^+$ to the log law; — (red), modified $\hat{U}_{mM}^+$ minus log law ((A6)); $\cdots$ (red), corrective term in (A6).

with

$$s_{1,2} = \left(-\frac{S}{2}\right)^{1/3} \left\{1 + \frac{2}{S(3\kappa_M)^3} \pm \left[1 + \frac{4}{S(3\kappa_M)^3}\right]^{1/2}\right\}^{1/3}, \tag{A2}$$

$$g_1 = s_1 + s_2 - \frac{1}{3\kappa_M}; \quad g_2 = -g_1 - \frac{1}{\kappa_M}; \tag{A3a,b}$$

$$g_3 = \frac{1}{4}\left(s_1 + s_2 + \frac{2}{3\kappa_M}\right)^2 + \frac{3}{4}(s_1 - s_2)^2; \quad g_4 = (4g_3 - g_2^2)^{1/2}, \tag{A3c,d}$$

$$\Gamma_1 = \frac{S + \kappa_M^{-1} g_1^2}{g_1^2 - g_1 g_2 + g_3}; \quad \Gamma_2 = \frac{1}{\kappa_M} - \Gamma_1; \quad \Gamma_3 = \frac{g_3 \Gamma_1 - S}{g_1}. \tag{A4a–c}$$

The additive log-law constant B_M is the limit $y^+ \to \infty$ of (A1)

$$B_M = -\Gamma_1 \ln(-g_1) - \frac{\Gamma_2}{2} \ln(g_2) + \frac{2\Gamma_3 + \Gamma_2 g_2}{g_4} \left[\frac{\pi}{2} + \arctan\left(\frac{g_2}{g_4}\right)\right], \tag{A5}$$

and its desired value is obtained by a simple iteration on S.

The basic Musker profile (A1) provides a good approximation to actual near-wall profiles with a logarithmic region at large y^+, but it also has shortcomings. One of them is the slow asymptotic approach to the log-law as $\hat{U}_M^+ \to \kappa_M^{-1} y^+ + B_M + \kappa_M^{-2}(y^+)^{-1} + O(y^+)^{-2}$. This defect is irrelevant when fitting experimental data, but is of concern for the higher-order asymptotic expansion of § 3. It is easily corrected by cancelling the $(y^+)^{-1}$ deviation of $\hat{U}_M^+$ from the log law at large y^+, resulting in the modified Musker profile

$$\hat{U}_{mM}^+(y^+; \kappa_M, B_M) = \hat{U}_M^+(y^+; \kappa_M, B_M) - (\kappa_M^2 y^+)^{-1} \exp(-100/y^+). \tag{A6}$$

As shown in figure 18, the effect is to ensure a clean log law for y^+ beyond approximately 150.

Another, more prominent, defect of the basic Musker profile is that it is too low in a region around y^+ of 30. This has first been described by Nagib & Chauhan (2008), who added to the Musker profile the 'hump' function

$$\hat{H}_{NC}(y^+; h_1, h_2, h_3) = h_1 \exp[-h_2 \ln^2(y^+/h_3)], \tag{A7}$$

with the original parameters $h_1 = 0.351$, $h_2 = 1$ and $h_3 = 30$. Their addition of a higher-order term, behaving as $-0.5\beta(y^+)^2/Re_\tau$ for $y^+ \to 0$ with β the pressure gradient

parameter, is, however, not consistent, if the Musker profile is used as an approximation for the leading order of the inner asymptotic expansion of U^+.

Appendix B. Comment on the dimensional analysis of Luchini (2017)

Luchini (2017) (see also Luchini 2018) has used dimensional analysis to derive a higher-order linear pressure gradient correction of the log law. His analysis is briefly summarized here to pinpoint where it goes wrong.

Luchini's application of the Buckingham Π theorem starts with the five dimensional variables $\{(\mathrm{d}\check{U}/\mathrm{d}\check{y}), \check{y}, \check{u}_\tau, (\partial\check{p}/\partial\check{x}), \check{\rho}\}$. One immediately notes that this starting list of variables implicitly contains the hydraulic diameter $\check{D}_H \equiv -4\check{\tau}_w(\partial\check{p}/\partial\check{x})^{-1}$, while Luchini explicitly excluded the other outer length scale $\check{L}$ (e.g. the channel half-height or pipe radius). From this starting list, two non-dimensional groupings are obtained,

$$\Pi_1 = \frac{\check{y}(\mathrm{d}\check{U}/\mathrm{d}\check{y})}{\check{u}_\tau}, \quad \Pi_2 = -\frac{\check{y}(\partial\check{p}/\partial\check{x})}{\check{\tau}_w} \equiv 4\frac{\check{y}}{\check{D}_H}, \qquad (B1a,b)$$

which are related by the functional relation $\Pi_1 = F(\Pi_2)$. Assuming that the function F is analytic around $\Pi_2 = 0$, Luchini Taylor-expanded F around $\Pi_2 = 0$ and truncated the series after the linear term $\propto \Pi_2$, which leads to (6) in Luchini (2017) and, after non-dimensionalization and integration with respect to y^+, to

$$U^+ = \kappa^{-1}\ln y^+ + B + 4A_1\frac{y^+}{D_H^+}. \qquad (B2)$$

It is between (6) and (7) of Luchini (2017) that the analysis goes wrong, when he replaces the single outer length scale D_H^+ in the last term of (B2) by $\beta(4L^+)^{-1}$ and implies that $\beta = 4L^+/D_H^+$ and L^+ can be chosen independently, in contradiction with the exclusion of $\check{L}$ from the list of starting variables for the Buckingham's Π theorem. In other words, (7) of Luchini (2017) is only valid for a fixed ratio of D_H^+ and $L^+ \equiv Re_\tau$, i.e. a fixed β.

Introducing also $\check{L}$ in the starting list of variables for the application of Buckingham's Π theorem adds a third $\Pi_3 = \beta$ to the list of the parameters (B1). As a consequence, nothing prevents the three parameters κ, B and A_1 in (B2) from becoming non-universal functions of β, as already suggested for κ and B by Nagib & Chauhan (2008), Monkewitz (2017) and Monkewitz (2019), for instance.

REFERENCES

AFZAL, N. & YAJNIK, K. 1973 Analysis of turbulent pipe and channel flows at moderately large Reynolds number. *J. Fluid Mech.* **61** (1), 23–31.

ALLEN, J.J., SHOCKLING, M.A. & SMITS, A.J. 2005 Evaluation of a universal transitional resistance diagram for pipes with honed surfaces. *Phys. Fluids* **17**, 121702.

AVSARKISOV, V., HOYAS, S., OBERLACK, M. & GARCÍA-GALACHE, J.P. 2014 Turbulent plane Couette flow at moderately high Reynolds number. *J. Fluid Mech.* **751**, R1.

BAILEY, S.C.C., *et al.* 2013 Obtaining accurate mean velocity measurements in high Reynolds number turbulent boundary layers using Pitot tubes. *J. Fluid Mech.* **715**, 642–670.

BAILEY, S.C.C., VALLIKIVI, M., HULTMARK, M. & SMITS, A.J. 2014 Estimating the value of von Kármán's constant in turbulent pipe flow. *J. Fluid Mech.* **749**, 79–98.

CHIN, C., MONTY, J.P. & OOI, A. 2014 Reynolds number effects in DNS of pipe flow and comparison with channels and boundary layers. *Intl J. Heat Fluid Flow* **45**, 33–40.

COLES, D.E. 1956 The law of the wake in the turbulent boundary layer. *J. Fluid Mech.* **1**, 191–226.

CRIGHTON, D.G. & LEPPINGTON, F.G. 1973 Singular perturbation methods in acoustics – diffraction by a plate of finite thickness. *Phil. Trans. R. Soc. Lond.* A **335**, 313.

DEL ÁLAMO, J.C., JIMÉNEZ, J., ZANDONADE, P. & MOSER, R.D. 2004 Scaling of the energy spectra of turbulent channels. *J. Fluid Mech.* **500**, 135–144.

EL KHOURY, G.K., SCHLATTER, P., NOORANI, A., FISCHER, P.F., BRETHOUWER, G. & JOHANSSON, A.V. 2013 Direct numerical simulation of turbulent pipe flow at moderately high Reynolds numbers. *Flow Turbul. Combust.* **91** (3), 475–495.

FIORINI, T. 2017 Turbulent pipe flow - high resolution measurements in CICLoPE. PhD thesis, University of Bologna.

FURUICHI, N., TERAO, Y., WADA, Y. & TSUJI, Y. 2018 Further experiments for mean velocity profile of pipe flow at high Reynolds number. *Phys. Fluids* **30**, 05510.

HOYAS, S. & JIMÉNEZ, J. 2006 Scaling of the velocity fluctuations in turbulent channels up to $Re_\tau = 2003$. *Phys. Fluids* **18**, 011702.

HULTMARK, M., VALLIKIVI, M., BAILEY, S.C. & SMITS, A.J. 2012 Turbulent pipe flow at extreme Reynolds numbers. *Phys. Rev. Lett.* **108**, 094501.

JIMÉNEZ, J. & MOSER, R.D. 2007 What are we learning from simulating wall turbulence? *Phil. Trans. R. Soc. Lond.* A **365** (1852), 715–732.

VON KÁRMÁN, T. 1930 Mechanische Ähnlichkeit und turbulenz (translation in NASA TM 611). *Nachr. Ges. Wiss. Göttingen, Math. Phys. Klasse* **5**, 58–76.

KEVORKIAN, J. & COLE, J.D. 1981 *Perturbation Methods in Applied Mathematics*. Springer.

KLEWICKI, J.C. 2013 A description of turbulent wall-flow vorticity consistent with mean dynamics. *J. Fluid Mech.* **737**, 176–204.

KRAHEBERGER, S., HOYAS, S. & OBERLACK, M. 2018 DNS of a turbulent Couette flow at constant wall transpiration up to $re_\tau = 1000$. *J. Fluid Mech.* **835**, 421–443.

LEE, M. & MOSER, R.D. 2015 Direct numerical simulation of turbulent channel flow up to $Re_\tau = 5200$. *J. Fluid Mech.* **774**, 395–415.

LEE, M. & MOSER, R.D. 2018 Extreme-scale motions in turbulent plane Couette flows. *J. Fluid Mech.* **842**, 128–145.

LOZANO-DURÁN, A. & JIMÉNEZ, J. 2014 Effect of the computational domain on direct numerical simulations of turbulent channels up to $Re_\tau = 4200$. *Phys. Fluids* **26**, 011702.

LUCHINI, P. 2017 Universality of the turbulent velocity profile. *Phys. Rev. Lett.* **118**, 224501.

LUCHINI, P. 2018 Structure and interpolation of the turbulent velocity profile in parallel flow. *Eur. J. Mech. (B/Fluids)* **71**, 15–34.

MARUSIC, I., MCKEON, B.J., MONKEWITZ, P.A., NAGIB, H.M., SMITS, A.J. & SREENIVASAN, K.R. 2010 Wall-bounded turbulent flows at high Reynolds numbers: recent advances and key issues. *Phys. Fluids* **22**, 065103.

MARUSIC, I. & MONTY, J.P. 2019 Attached Eddy model of wall turbulence. *Annu. Rev. Fluid Mech.* **51** (1), 49–74.

MARUSIC, I., MONTY, J.P., HULTMARK, M. & SMITS, A.J. 2013 On the logarithmic region in wall turbulence. *J. Fluid Mech. Rapids* **716**, R3–1–R3–11.

MCKEON, B.J. 2003 High Reynolds number turbulent pipe flow. PhD thesis, Princeton University.

MCKEON, B.J., LI, J., JIANG, W., MORRISON, J.F. & SMITS, A.J. 2004 Further observations on the mean velocity distribution in fully developed pipe flow. *J. Fluid Mech.* **501**, 135–147.

MILLIKAN, C.M. 1938 A critical discussion of turbulent flows in channels and circular tube. In *Proceedings of the 5th ICTAM, Harvard University and MIT, (USA)* (ed. J.P. den Hartog & H. Peters), pp. 386–392. John Wiley and Sons, Inc.

MONKEWITZ, P.A. 2017 Revisiting the quest for a universal log-law and the role of pressure gradient in "canonical" wall-bounded turbulent flows. *Phys. Rev. Fluids* **2**, 094602.

MONKEWITZ, P.A. 2019 Derivation of pitot corrections for the Zagarola & Smits Superpipe data and their composite fit. arXiv:1902.03829v1.

MONKEWITZ, P.A., CHAUHAN, K.A. & NAGIB, H.M. 2007 Self-consistent high-Reynolds-number asymptotics for zero-pressure-gradient turbulent boundary layers. *Phys. Fluids* **19**, 115101.

MONKEWITZ, P.A. & NAGIB, H.M. 2015 Large Reynolds number asymptotics of the stream-wise normal stress in ZPG turbulent boundary layers. *J. Fluid Mech.* **783**, 474–503.

MONKEWITZ, P.A., NAGIB, H.M. & BOULANGER, V. 2017 Comparing the three possible scalings of stream-wise normal stress in turbulent boundary layers. In *Proceedings - TSFP10, Chicago, (USA)* (ed. A.J. Smits & H.M. Nagib). Available at: http://www.tsfp-conference.org.

MONTY, J.P. 2005 Developments in smooth wall turbulent duct flows. PhD thesis, University of Melbourne.

MUSKER, A.J. 1979 Explicit expression for the smooth wall velocity distribution in a turbulent boundary layer. *AIAA J.* **17**, 655–657.

NAGIB, H.M. & CHAUHAN, K.A. 2008 Variations of von Kármán coefficient in canonical flows. *Phys. Fluids* **20**, 101518.

NAGIB, H.M., MONKEWITZ, P.A., MASCOTELLI, L., BELLANI, G. & TALAMELLI, A. 2019 Uncertainty analysis of the von Kármán constant for the mean centerline velocity in CICLoPE. In *Progress in Turbulence VIII* (ed. Örlü *et al.*). Springer Nature.

NAGIB, H.M., MONKEWITZ, P.A., MASCOTELLI, L., FIORINI, T., BELLANI, G., ZHENG, X. & TALAMELLI, A. 2017 Centerline Kármán constant revisited and contrasted to log-layer Kármán constant at ciclope. In *Proceedings - TSFP10, Chicago, (USA)* (ed. A.J. Smits & H.M. Nagib). Available at: http://www.tsfp-conference.org.

OBERLACK, M. 2001 A unified approach for symmetries in plane parallel turbulent shear flows. *J. Fluid Mech.* **427**, 299–328.

PANTON, R.L. 2005 Review of wall turbulence as described by composite expansions. *Appl. Mech. Rev.* **58** (1), 1–36.

PANTON, R.L., LEE, M. & MOSER, R.D. 2017 Correlation of pressure fluctuations in turbulent wall layers. *Phys. Rev. Fluids* **2**, 094604.

PERRY, A.E. & ABELL, C.J. 1977 Asymptotic similarity of turbulence structures in smooth- and rough-walled pipes. *J. Fluid Mech.* **79**, 785–799.

PERRY, A.E., HAFEZ, S. & CHONG, M.S. 2001 A possible reinterpretation of the Princeton superpipe data. *J. Fluid Mech.* **439**, 395–401.

PIROZZOLI, S., BERNARDINI, M. & ORLANDI, P. 2014 Turbulence statistics in Couette flow at high Reynolds number. *J. Fluid Mech.* **758**, 327–343.

POPE, S.B. 2000 *Turbulent Flows*. Cambridge University Press.

SCHULTZ, M.P. & FLACK, K.A. 2013 Reynolds number scaling of turbulent channel flow. *Phys. Fluids* **25**, 025104.

SREENIVASAN, K.R. & SAHAY, A. 1997 The persistence of viscous effects in the overlap region, and the mean velocity in turbulent pipe and channel flows. In *Self-Sustaining Mechanism of Wall Turbulence* (ed. R.L. Panton), pp. 253–271. Computational Mechanics Publications.

THAIS, L., MOMPEAN, G. & GATSKI, T. 2013 Spectral analysis of turbulent viscoelastic and newtonian channel flows. *J. Non-Newtonian Fluid Mech.* **200**, 165–176.

TSUKAHARA, T., KAWAMURA, H. & SHINGAI, K. 2006 DNS of turbulent Couette flow with emphasis on the large-scale structure in the core region. *J. Turbul.* **7**, N19.

VINUESA, R., DUNCAN, R.D. & NAGIB, H.M. 2016 Alternative interpretation of the superpipe data and motivation for ciclope: the effect of decreasing viscous length scale. *Eur. J. Mech. (B/Fluids)* **58**, 109–116.

VINUESA, R., SCHLATTER, P. & NAGIB, H.M. 2018 Secondary flow in turbulent ducts with increasing aspect ratio. *Phys. Rev. Fluids* **3**, 054606.

WEI, T., FIFE, P., KLEWICKI, J. & MCMURTRY, P. 2005 Properties of the mean momentum balance in turbulent boundary layer, pipe and channel flows. *J. Fluid Mech.* **522**, 303–327.

WU, X. & MOIN, P. 2008 A direct numerical simulation study on the mean velocity characteristics in turbulent pipe flow. *J. Fluid Mech.* **608**, 81–112.

YAJNIK, K.S. 1970 Asymptotic theory of turbulent shear flows. *J. Fluid Mech.* **42** (2), 411–427.

ZAGAROLA, M.V. & SMITS, A.J. 1997 Scaling of the mean velocity profile for turbulent pipe flow. *Phys. Rev. Lett.* **78**, 239–242.

ZAGAROLA, M.V. & SMITS, A.J. 1998 Mean-flow scaling of turbulent pipe flow. *J. Fluid Mech.* **373**, 33–79.

ZANOUN, E.S., DURST, F., BAYOUMY, O. & AL-SALAYMEH, A. 2007 Wall skin friction and mean velocity profiles of fully developed turbulent pipe flows. *Exp. Therm. Fluid Sci.* **32** (1), 249–261.

ZANOUN, E.S., DURST, F. & NAGIB, H.M. 2003 Evaluating the law of the wall in two-dimensional fully developed turbulent channel flows. *Phys. Fluids* **15**, 3079–3089.